1   Subventricular zone cytogenesis provides trophic support for neural repair

2

3   Michael R. Williamson[1*], Stephanie P. Le[2], Ronald L. Franzen[2], Nicole A. Donlan[2], Jill L.

4   Rosow[2], Andrew K. Dunn[1,3], Theresa A. Jones[1,2], Michael R. Drew[1,4]

5

6   [1]Institute for Neuroscience

7   [2]Department of Psychology

8   [3]Department of Biomedical Engineering

9   [4]Center for Learning and Memory and Department of Neuroscience

10   University of Texas at Austin, Austin, Texas, USA, 78712

11

12   *Correspondence:

13   Michael R. Williamson

14   1 University Station, C7000, Austin, TX, 78712

15   mrwillia@utexas.edu

Abstract

Stroke enhances proliferation of neural precursor cells within the subventricular zone (SVZ) and induces ectopic migration of newborn cells towards the site of injury. Here we characterize the identity of cells arising from the SVZ after stroke and provide insight into their function by uncovering a mechanism through which they facilitate neural repair and functional recovery. Using genetic lineage tracing, we show that SVZ-derived cells that migrate towards stroke-induced cortical lesions in mice are predominantly undifferentiated precursors, suggesting that the main function of post-injury cytogenesis is not cell replacement. We find that SVZ-derived cells are a unique cellular source of trophic factors that instruct neural repair. Chemogenetic ablation of neural precursor cells or conditional knockout of VEGF in the adult neural stem cell lineage impairs neuronal and vascular reparative responses and worsens functional recovery after stroke. In addition, normal aging markedly diminishes the cytogenic response to stroke, resulting in worse functional recovery. Therapeutic replacement of VEGF in peri-infarct cortex is sufficient to induce neural repair and functional recovery in mice with arrested cytogenesis. These findings indicate that the SVZ cytogenic response following brain injury is a source of trophic support that drives neural repair and recovery.

Introduction

Limited recovery of function occurs after damage to the central nervous system. Consequently, stroke and other forms of brain injury often cause long-lasting disabilities. Following stroke, remodeling of residual tissue surrounding the site of injury is thought to underlie recovery. For example, extensive plasticity of neural circuits and blood vessels occurs in peri-infarct regions and these processes are associated with functional improvement (Brown et al., 2007; Clark et al., 2019; Tennant et al., 2017; Williamson et al., 2020). Repair processes are mediated by interactions across disparate cell types (Brown et al., 2007; Clark et al., 2019; Joy et al., 2019; Kim et al., 2018; Williamson et al., 2021). However, the intercellular interactions that orchestrate repair and recovery remain to be completely defined. A more complete understanding of the mechanisms that govern neural repair could inform development of new treatment strategies.

Cytogenesis, the formation of new cells, is limited in the adult mammalian brain. The subventricular zone (SVZ) is one of a small number of regions that contains multipotent neural stem and progenitor cells (collectively referred to here as precursors) that generate new neurons and glia in adulthood (Doetsch et al., 1999; Garcia et al., 2004). Normally, the predominant progeny arising from the SVZ are new neurons that migrate towards the olfactory bulb and integrate into existing olfactory circuitry. However, injuries such as stroke markedly increase SVZ precursor proliferation and induce ectopic migration of SVZ-derived cells towards the site of injury (Arvidsson et al., 2002; Lagace, 2012; Li et al., 2010; Ohab et al., 2006; Parent et al., 2002; Williamson et al., 2019). Past studies of this process after brain injury have largely focused on neurogenesis — the formation of new neurons and their localization in peri-infarct regions (Arvidsson et al., 2002; Parent et al., 2002). In general, experimental manipulations that increase

59   post-stroke neurogenesis are associated with enhanced functional recovery (Lagace, 2012). The

60   prevailing view has been that cell replacement, especially neuron replacement, by SVZ

61   precursors allows for partial brain regeneration and consequently improved function. However,

62   recent findings indicate that new neurons poorly integrate into existing circuits in peri-infarct

63   regions and receive little synaptic input (Kannangara et al., 2018), making their functional

64   importance unclear (cf. Liang et al., 2019). Moreover, other studies have found that glia

65   outnumber neurons among migrating SVZ-derived cells, but the entire population of SVZ-

66   derived cells has yet to be comprehensively characterized (Benner et al., 2013; Faiz et al., 2015;

67   Li et al., 2010). Overall, the identity and functional importance of new cells that arise from the

68   SVZ after injury are not well understood.

69   Here we investigate the SVZ cytogenic response following cortical photothrombotic

70   strokes in mice. Our goals were to characterize the types of cells produced by the SVZ after

71   stroke and mechanistically understand the role of SVZ cytogenesis in stroke recovery. We use

72   indelible lineage tracing to phenotype SVZ-derived cells that migrate towards the site of injury.

73   Unexpectedly, we find that the majority of these cells are undifferentiated precursors, suggesting

74   that cell replacement is limited. Reducing cytogenesis impairs motor recovery after stroke, at

75   least in part due to deficits in neuronal and vascular plasticity. With gain- and loss-of-function

76   manipulations, we show that VEGF produced by SVZ-derived cells drives repair and functional

77   recovery. These findings identify SVZ cytogenesis as a source of trophic support that facilitates

78   neural repair. Thus, our study demonstrates a mechanism other than cell replacement by which

79   endogenous neural precursor cells contribute to repair and recovery in the injured central nervous

80   system.

81

4

82 **Results**

83 *Cells arising from the subventricular zone after stroke are predominantly quiescent precursors*

84 *and astrocytes*

85   We used genetic lineage tracing to characterize the SVZ cytogenic response to stroke.

86 Young adult (3-6 months old) *Nestin-CreER*; Ai14 mice were injected with tamoxifen to induce

87 indelible tdTomato expression in neural stem cells and their progeny (Figure 1A, B) (Benner et

88 al., 2013; Li et al., 2010). Four weeks later, photothrombotic cortical infarcts were induced, and

89 tissue was collected two weeks post-stroke, which is a time when large numbers of SVZ-derived

90 cell are localized to peri-infarct cortex, substantial neural repair is ongoing, and functional

91 improvement is incomplete (Kannangara et al., 2018; Kim et al., 2018; Williamson et al., 2021).

92 While no cortical migration was seen in the absence of injury, unilateral strokes induced a

93 profound migration of tdTomato$^+$ cells from the SVZ into peri-infarct cortex (Figure 1C, D). We

94 immunostained tissue to examine expression of an array of differentiation stage-specific and

95 proliferation-associated proteins in lineage-traced cells (Figure 1E-Q, Supplemental Figure 1,

96 Supplemental Figure 2).

97   Unexpectedly, the majority of tdTomato$^+$ cells in peri-infarct cortex expressed precursor

98 cell-associated markers (93.8±1.1% were CD133$^+$, 92.9±1.1% were Sox2$^+$, and 66.2±0.7% were

99 Ascl1$^+$). 27.1±1.9% of tdTomato$^+$ cells were differentiated astrocytes based on expression of

100 S100β, which defines astrocyte maturation and loss of multipotency (Lattke et al., 2021; Raponi

101 et al., 2007) and is not expressed by SVZ precursors (Codega et al., 2014). Astrocyte reactivity is

102 associated with re-expression of some precursor cell-associated proteins, including CD133 and

103 Sox2 (Götz et al., 2015; Robel et al., 2011), but reactive astrocytes do not express Ascl1

5

104   (Magnusson et al., 2014; Zamboni et al., 2020). Thus, the Ascl1^{+} subpopulation defined

105   undifferentiated precursors, the S100β[+] subpopulation defined astrocytes, and CD133/Sox2

106   labeled both subpopulations (Figure 1E). Lineage-traced cells were largely quiescent as defined

107   by expression of the quiescence marker Id2 in 92.1±1.5% of cells (Llorens-Bobadilla et al.,

108   2015), and rare expression of the proliferation marker Ki67 (4.1±1.5%). Oligodendrocyte-lineage

109   (Olig2^{+}, 4.1±0.5%) and neuron-lineage cells (DCX[+], 3.0±0.6%, and NeuN[+], 0.9±0.7%; (also see

110   Supplemental Figure 2)) made up the remainder of lineage-traced cells. We corroborated these

111   phenotyping results with parallel experiments in *Ascl1-CreER*; Ai14 mice, in which a subset of

112   neural stem and progenitor cells are lineage-traced (Liang et al., 2019) (Supplemental Figure 1).

113   We also confirmed that few new neurons are formed up to 6 weeks post-stroke using *Nestin-*

114   *CreER*; *Sun1-sfGFP^fl* mice in which neural stem cells and their progeny were labeled with a

115   nuclear membrane-targeted fluorophore (Supplemental Figure 2). These experiments identify

116   undifferentiated precursors as the predominant cell type produced by the SVZ in response to

117   stroke. Since the majority of new cells that localize to peri-infarct regions remain in an

118   undifferentiated state, cell replacement may not be the primary function of the cytogenic

119   response.
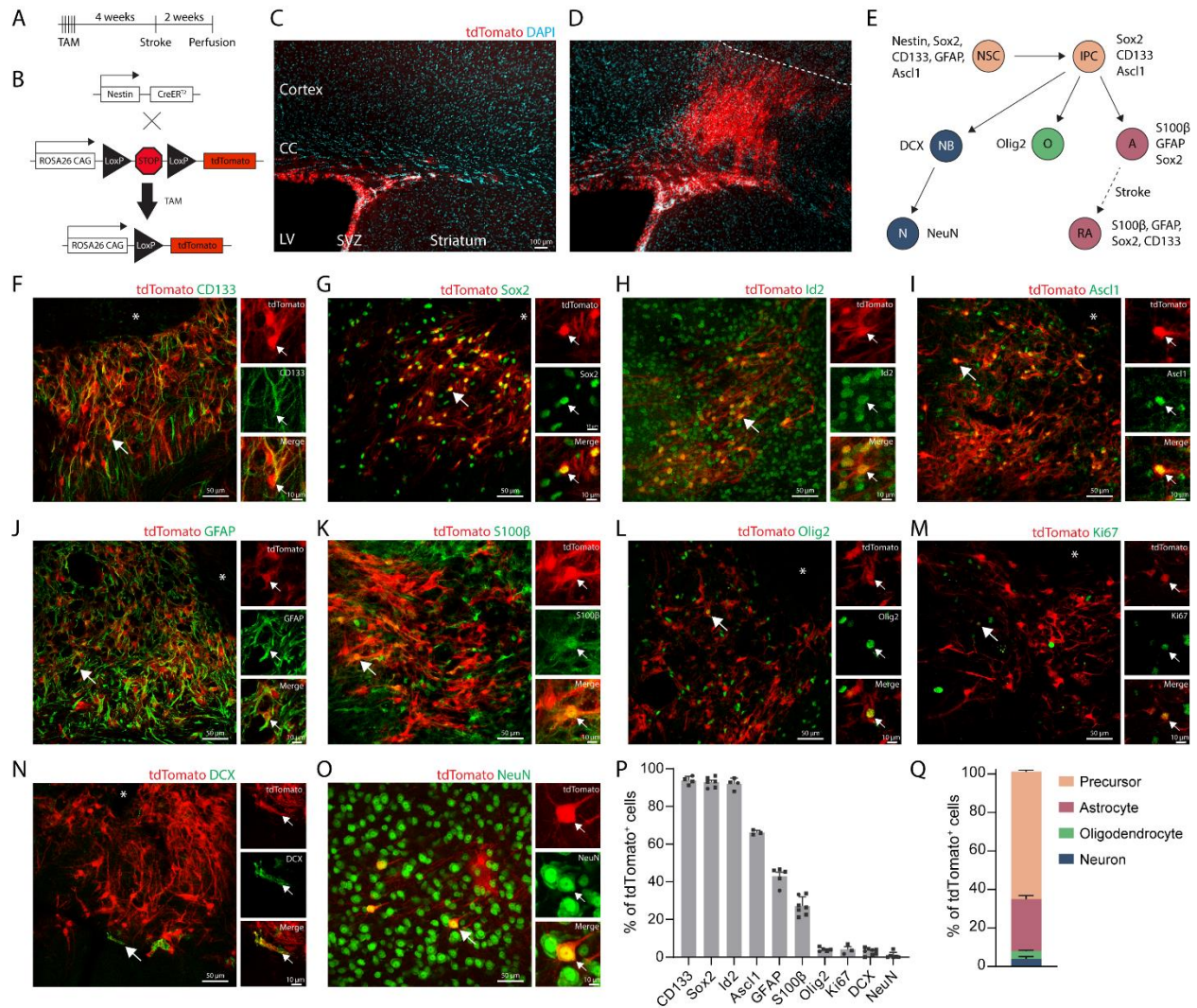
Figure 1. SVZ-derived cells are predominantly undifferentiated precursors and astrocytes.

A) Experimental timeline for lineage tracing neural stem cell progeny after stroke. Tissue was collected two weeks post-stroke. B) Schematic of inducible, neural stem cell-specific lineage tracing system in Nestin-CreER; Ai14 mice. Tamoxifen (TAM) administration induces tdTomato expression in neural stem cells and their progeny. C) Image of tdTomato-expressing cells in the subventricular zone in the absence of injury. Note the lack of cortical migration of tdTomato$^+$ cells. CC, corpus callosum; LV, lateral ventricle; SVZ, subventricular zone. D) Substantial migration of tdTomato$^+$ cells towards the infarct after cortical photothrombotic stroke (dashed line indicates the approximate infarct border). E) Schematic of differentiation stages as defined by marker expression. Neural stem cells (NSC) produce intermediate progenitor cells (IPC), which give rise to cells of the three major neural lineages: neurons (NB, neuroblast; N, neuron), oligodendrocytes (O), and astrocytes (A). After stroke, reactive astrocytes (RA) re-express some neural stem cell markers. F-O) Representative confocal images of tdTomato$^+$ cells and immunostaining for lineage and functional markers. Images are from peri-infarct cortex two weeks post-stroke. Asterisks indicate the lesion core. Most tdTomato$^+$ cells (precursors and

7

136   astrocytes) expressed the stem cell-associated markers CD133 (F) and Sox2 (G), and the
137   quiescence marker Id2 (H). $Id2^+$ tdTomato$^-$ cells include mature resident cortical cells.
138   Undifferentiated precursors were uniquely identified by expression of Ascl1 (I). J) GFAP
139   marked astrocytes and a subset of precursors. K) Differentiated astrocytes were defined by
140   expression of S100β. L) The oligodendrocyte lineage was defined by Olig2 expression. M) Few
141   cells expressed the proliferation marker Ki67. Neuron lineage cells, DCX^+ (N) and $NeuN^+$ (O),
142   were the least common. P) Quantification of marker expression by $tdTomato^+$ cells. Data are
143   from n = 3-8 mice per marker, and > 100 $tdTomato^+$ cells counted per mouse per marker. Q)
144   Estimate of phenotype distribution of lineage traced cells. Precursors were defined by Ascl1
145   expression. Astrocytes were defined by S100β expression. Oligodendrocyte lineage was defined
146   by Olig2 expression. Neuron lineage was defined by DCX and NeuN expression. See also
147   Supplemental Figure 1 and Supplemental Figure 2. Data are presented as mean ± SEM.
148   Datapoints representing males are shown as circles; datapoints representing females are shown as
149   squares.

150

151   *Chemogenetic ablation of neural stem cells impairs recovery after stroke*

152   Having characterized the phenotype of SVZ-derived cells, we next investigated whether

153   SVZ cytogenesis provides functional benefits for recovery after stroke. We used GFAP-TK mice

154   to selectively ablate neural stem cells prior to stroke following an established ganciclovir (GCV)

155   administration paradigm (Garcia et al., 2004; Swan et al., 2014) (Figure 2A-J). Delivery of GCV

156   via subcutaneous osmotic pumps for two weeks ablates mitotic TK-expressing cells (i.e. neural

157   stem cells), but spares non-mitotic GFAP-expressing cells, including cortical astrocytes (Garcia

158   et al., 2004; Swan et al., 2014) (Figure 2D-F; Supplemental Figure 3A-C). SVZ cytogenesis, as

159   measured by the density of SVZ DCX^+ and $Ki67^+$ cells, was substantially reduced in GFAP-

160   TK+GCV mice relative to littermate controls, which included wildtype mice given saline or

161   GCV and GFAP-TK mice given saline (Figure 2G-J).

162   Following GCV administration, we compared motor recovery between GFAP-TK mice

163   and wildtype littermates after photothrombotic cortical infarcts targeting the forelimb area of

164   motor cortex (Tennant et al., 2011; Williamson et al., 2021) (Figure 2K). Motor function was

8

165   assessed with the single seed reaching task, a highly sensitive and translationally relevant

166   measure of skilled reaching (Klein et al., 2012; van Lieshout et al., 2021). There was no

167   difference between groups in reaching performance during pre-stroke GCV delivery (Bonferroni-

168   corrected p > 0.999). Mice lacking cytogenesis showed significantly worse recovery out to four

169   weeks following stroke (Figure 2L). Lesion size and location did not differ between groups

170   (Figure 2M, N). These results demonstrate that SVZ cytogenesis promotes functional recovery

171   after stroke.

172
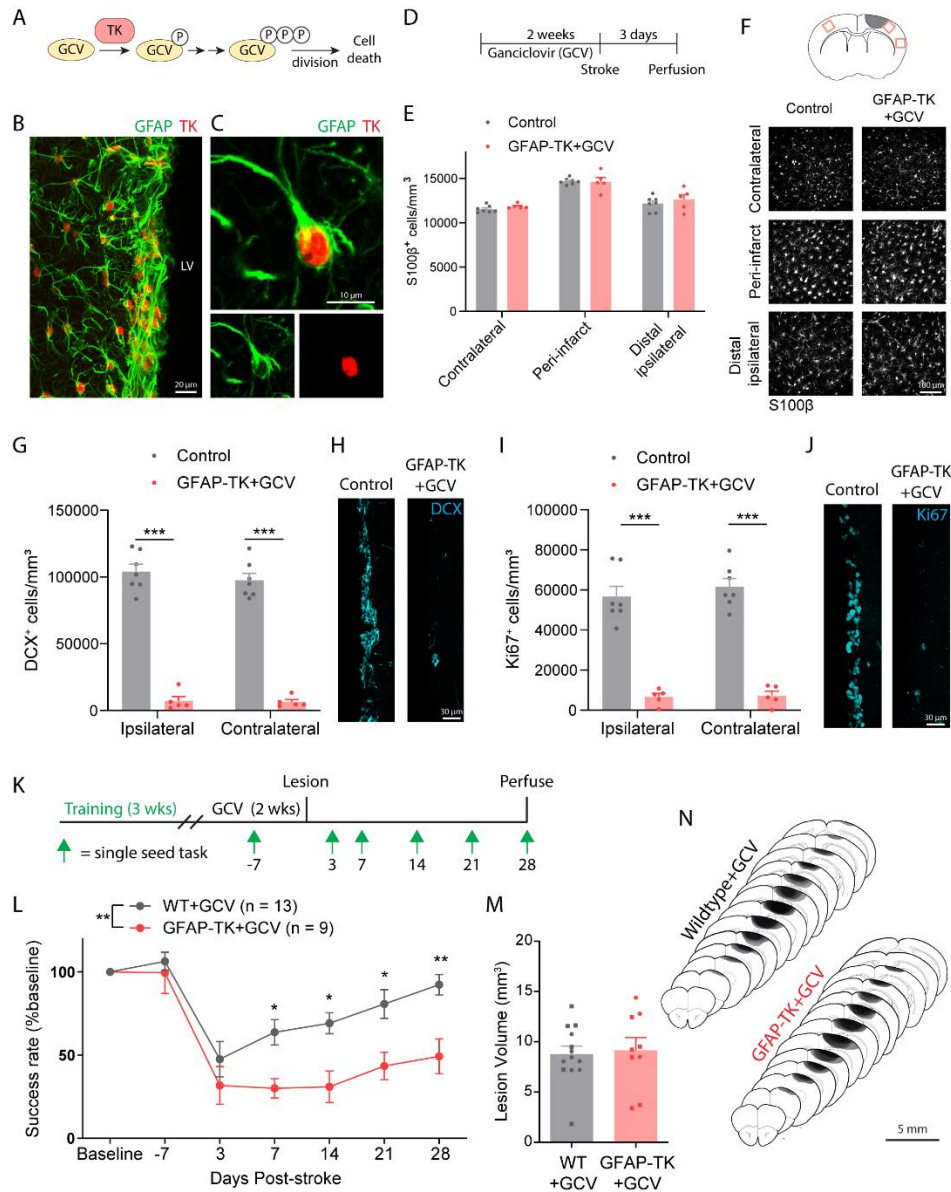
Figure 2. Ablation of neural stem cells worsens recovery after stroke.

A) Schematic illustrating the thymidine kinase (TK)/ganciclovir (GCV) system for conditional ablation of proliferating cells. B) Confocal image showing TK expression in GFAP$^+$ cells of the subventricular zone in a GFAP-TK mouse. LV, lateral ventricle. C) High-resolution image of a TK-expressing SVZ stem cell. D) Experimental timeline for assessing the specificity and effectiveness of arresting SVZ cytogenesis with GFAP-TK mice (E-J). GCV or saline was delivered for 14 days via osmotic pump. Tissue was collected 3 days after stroke. n = 7 control (wildtype mice given GCV or GFAP-TK mice given saline), n = 5 GFAP-TK+GCV. E) Parenchymal astrocytes were not depleted in this paradigm. t(10) < 1.53, p ≥ 0.157, t tests comparing groups for each region. F) Representative images of S100β$^+$ cells from three cortical

183 regions (see diagram at top) show lack of astrocyte ablation. G-J) GFAP-TK mice permit
184 conditional arrest of cytogenesis. The number of SVZ DCX$^+$ (G, H) and Ki67$^+$ cells (I, J) was
185 significantly reduced in GFAP-TK mice given GCV relative to controls. ***$t(10) \geq 7.99$, p <
186 0.001, t tests. K) Experimental design for assessing motor recovery after photothrombotic stroke
187 with the single seed reaching task (n = 13 wildtype (WT), n = 9 GFAP-TK). L) Arrest of
188 cytogenesis significantly worsened recovery of motor function. Time x group interaction F(6,
189 120) = 3.61, p = 0.0025. *p < 0.05, **p < 0.01, Bonferroni tests. M) Lesion volume was not
190 different between groups. t(20) = 0.27, p = 0.787. N) Lesion reconstruction. Darker shades
191 represent more overlap between animals. Data are presented as mean ± SEM. Where individual
192 datapoints are shown, datapoints representing males are shown as circles; datapoints representing
193 females are shown as squares.

194

195 *Aging diminishes the SVZ cytogenic response to stroke and its functional benefits*

196   Aging is associated with a substantially higher incidence of stroke (Kissela et al., 2012)

197 and reduced recovery of function (Paolucci et al., 2003). In animals, aging is associated with

198 diminished SVZ cytogenesis (Bouab et al., 2011; Jin et al., 2004; Kalamakis et al., 2019; Luo et

199 al., 2006). We examined the impact of aging on normal and post-stroke SVZ cytogenesis by

200 comparing young adult (aged 3-6 months) and aged (12-16 months) *Nestin-CreER*; Ai14 mice.

201 Mice were either uninjured (naïve) or subjected to cortical stroke two weeks prior to tissue

202 collection. In young mice, stroke increased the number of Ki67$^+$ proliferative cells and

203 tdTomato$^+$Sox2$^+$ precursors in the SVZ relative to young naïve, aged naïve, and aged stroke mice

204 (Figure 3A-D). By contrast, in aged mice, there was no significant difference in the number of

205 SVZ Ki67$^+$ or tdTomato$^+$Sox2$^+$ cells after stroke relative to naïve mice (p = 0.604, p = 0.998,

206 respectively, Tukey tests). Thus, stroke increases SVZ proliferation and expands the precursor

207 cell pool in young, but not aged, mice.

208   We next examined the effects of aging on the migratory response of lineage-traced SVZ

209 cells after stroke. The density of tdTomato$^+$ cells in peri-infarct cortex two weeks post-stroke

210 was about five-fold lower in aged mice relative to young mice (Figure 3E, F). Despite the

211   diminished cytogenic response, the phenotype distribution of tdTomato$^+$ cells in peri-infarct

212   cortex of aged mice (Figure 3G) was similar to what we observed in young adult mice (Figure 1),

213   with the majority of cells identified as precursors and astrocytes. Thus, far fewer SVZ-derived

214   cells localize to peri-infarct regions in aged mice, but their phenotype distribution is similar to

215   that of young mice.

216   We next investigated whether the blunted cytogenic response observed in aged mice was

217   still functionally beneficial (Figure 3H). We used GFAP-TK mice to selectively ablate neural

218   stem cells prior to stroke. BrdU pulse labeling of proliferating cells revealed a near complete loss

219   of BrdU$^+$ cells in the SVZ of GFAP-TK+GCV mice relative to control aged mice (Figure 3I, J;

220   all mice aged 12-16 months). We assessed motor recovery with the single-seed task and found no

221   differences between groups (Figure 3K). Notably, both aged groups performed significantly

222   worse on day 28 than young mice within intact cytogenesis (data from Figure 2; $F(3, 35) = 7.46$,

223     $p < 0.001$ one-way ANOVA; $p < 0.012$, Tukey tests), but similarly to young GFAP-TK+GCV

224   mice ($p > 0.978$, Tukey tests). Lesion size was not different between aged groups (Figure 3L,

225   M), and was similar to that of young adults (Figure 2M, N). Altogether, our results indicate that

226   aging diminishes the cytogenic response to stroke and its functional benefits. Together with our

227   findings in young mice, our results show that reduced SVZ cytogenesis, by neural stem cell

228   ablation or aging, is associated with worse functional recovery. Reduced cytogenesis may

229   contribute to worse outcome after stroke with aging.

12

230
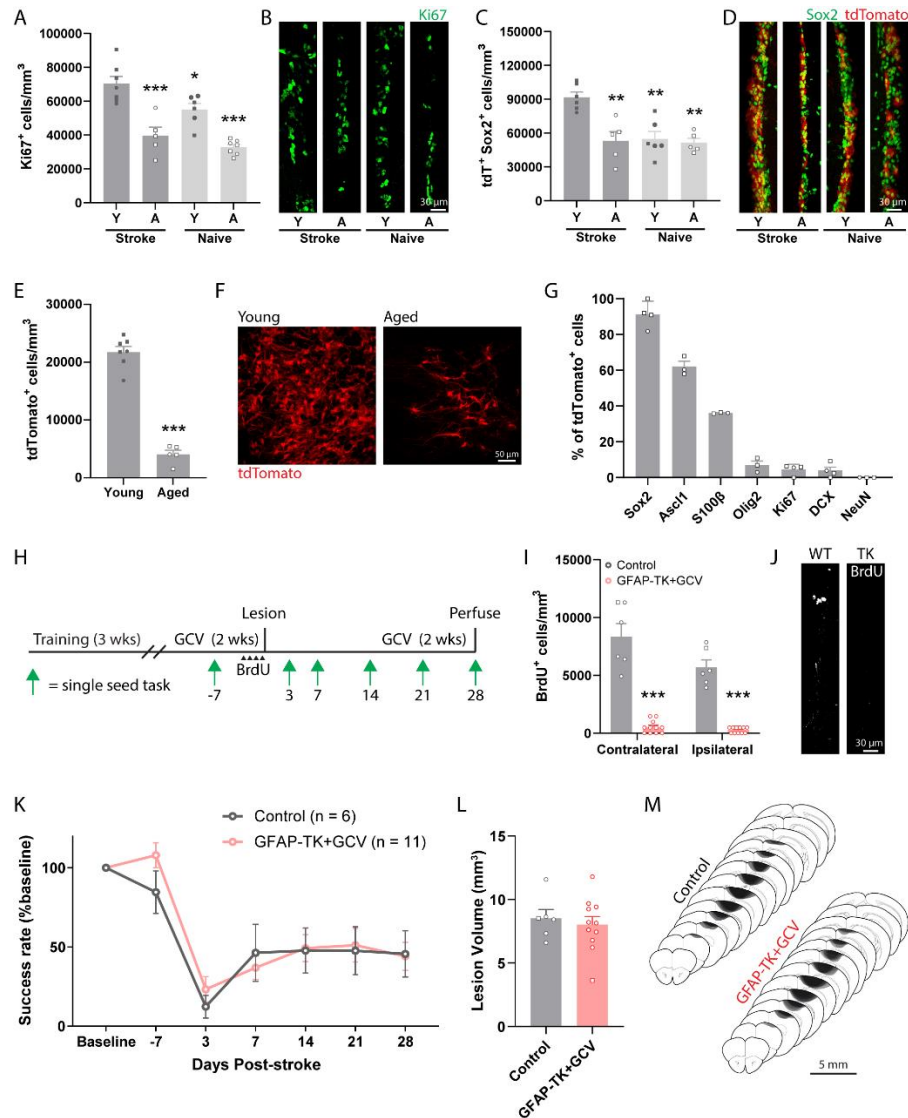
Figure 3. Aging diminishes the cytogenic response to stroke and its contribution to recovery.

A-D) Assessment of SVZ cytogenesis in young (Y, 3-6 months) and aged (A, 12-16 months) Nestin-CreER; Ai14 mice (n = 5-7 mice/group). Tissue was collected two weeks post-stroke. The number of proliferating cells (Ki67$^+$, A and B) and neural precursor cells (tdTomato$^+$ Sox2$^+$, C and D) in the SVZ was significantly higher in young mice after stroke compared to all other groups. *$p < 0.05$, ** $p < 0.01$, ***$p < 0.001$ relative to young stroke mice, Tukey tests. E) Fewer tdTomato$^+$ cells were observed in peri-infarct cortex of aged mice two weeks post-stroke. ***$t(10) = 13.4$, $p < 0.001$. F) Representative images of tdTomato$^+$ cells in peri-infarct cortex. G) Quantification of lineage marker expression by tdTomato$^+$ cells in peri-infarct cortex of aged mice at two weeks post-stroke (n = 3-4 mice per marker). Similar to what was observed in young mice (Figure 1), most SVZ-derived cells were undifferentiated precursors or astrocytes. H) Experimental timeline for examining the effects of neural stem cell ablation in aged mice (n = 6

13

244 controls, n = 11 GFAP-TK given GCV). I) GFAP-TK+GCV mice had fewer BrdU$^+$ cells in the

245 SVZ, validating stem cell ablation. ***t(15) ≥ 9.36, p < 0.001. BrdU was given twice per day for

246 two days prior to stroke. J) Representative images of BrdU immunostaining in the SVZ. K) Both

247 aged controls and GFAP-TK+GCV mice showed poor recovery following stroke. There was no

248 difference between groups. Group main effect F(1,15) = 0.17, p = 0.690. L) Lesion volume was

249 not different between groups (t(15) = 0.50, p = 0.628). M) Lesion reconstruction. Darker shades

250 represent more overlap between animals. Data are presented as mean ± SEM. Where individual

251 datapoints are shown, datapoints representing males are shown as circles; datapoints representing

252 females are shown as squares.

253

254 *Arrest of cytogenesis disrupts neuronal and vascular repair*

255   Our results indicate that most SVZ-derived cells are undifferentiated precursors and

256 reactive astrocytes. We hypothesized that these cell types may influence repair processes to

257 promote behavioral improvement. In particular, synaptic plasticity and vascular remodeling are

258 two functionally important aspects of neural repair that could potentially be augmented by

259 factors produced by SVZ-derived cells. Indeed, past studies have demonstrated beneficial effects

260 of transplanted stem cells and resident cortical astrocytes on these processes (Andres et al., 2011;

261 Bacigaluppi et al., 2016; Horie et al., 2011; Lin et al., 2017; Llorente et al., 2021; Pluchino et al.,

262 2005; Roitbak et al., 2011; Sabelström et al., 2013; Williamson et al., 2021).

263   We investigated the consequences of neural stem cell ablation on synaptic and vascular

264 plasticity in residual cortex surrounding photothrombotic infarcts with a longitudinal imaging

265 approach (Figure 4A, B). We bred GFAP-TK mice with Thy1-GFP mice, which have sparse,

266 GFP-labeled pyramidal neurons. Resulting double transgenic mice allowed us to monitor

267 synaptic remodeling at single-synapse resolution with repeated 2-photon imaging of dendritic

268 spines on apical dendrites before and after stroke (Brown et al., 2007; Clark et al., 2019;

269 Mostany et al., 2010) with the ability to conditionally arrest cytogenesis. Blood flow was tracked

270 with multi-exposure speckle imaging (MESI), a quantitative, optical, contrast-free technique that

271   yields high-resolution blood flow maps (He et al., 2020; Williamson et al., 2020). Prior to stroke,

272   control and TK$^{+/-}$ mice were unilaterally implanted with cranial windows, trained on the single-

273   seed reaching task, administered GCV or saline, and subjected to baseline imaging. We then

274   induced strokes in forelimb motor cortex and periodically imaged dendritic spines and blood

275   flow and assessed behavioral performance during recovery.

276   Motor recovery was again significantly impaired in GFAP-TK+GCV mice, with no

277   differences in lesion size observed between groups (Figure 4C-E). 2-photon imaging of dendritic

278   spines revealed increased spine turnover in peri-infarct cortex (Figure 4F-H), consistent with past

279   work (Brown et al., 2007; Clark et al., 2019; Joy et al., 2019; Mostany et al., 2010). There were

280   no group differences in spine dynamics before stroke (Supplemental Figure 4). New spine

281   formation peaked during the second week after stroke, and was significantly higher in mice with

282   intact cytogenesis. Spine elimination was greatest during the first week post-stroke, and

283   subsequently declined with time, without significant differences between groups. A

284   subpopulation of new spines formed after stroke persists long-term, and the persistence of newly

285   formed spines is associated with greater functional recovery (Clark et al., 2019). The survival of

286   new spines was significantly reduced in GFAP-TK+GCV mice regardless of the day of spine

287   formation (Figure 4I). Moreover, spine survival rate was positively correlated with behavioral

288   performance on the final assessment day (Figure 4J). Thus, SVZ cytogenesis supports synaptic

289   remodeling after stroke, particularly by promoting the long-term stabilization of new synapses.

290   Broad regions of reduced blood flow persist for days to weeks surrounding focal strokes

291   (He et al., 2020; Williamson et al., 2020). Remodeling of peri-infarct vasculature helps to restore

292   blood flow and is associated with behavioral improvement (Williamson et al., 2020). To examine

293   vascular remodeling, we injected mice with fluorophore-conjugated tomato lectin immediately

294   before euthanasia to label perfused vasculature. Vessel density in peri-infarct cortex was

295   significantly reduced in GFAP-TK+GCV mice relative to controls (Figure 4K, L). Furthermore,

296   longitudinal blood flow imaging demonstrated impaired recovery of blood flow at days 5 and 28

297   post-stroke (Figure 4M, N). Early vascular permeability was not affected by arresting

298   cytogenesis (Supplemental Figure 3). Overall, these findings demonstrate that SVZ-derived cells

299   beneficially shape neuronal and vascular remodeling processes after stroke in order to promote

300   recovery.
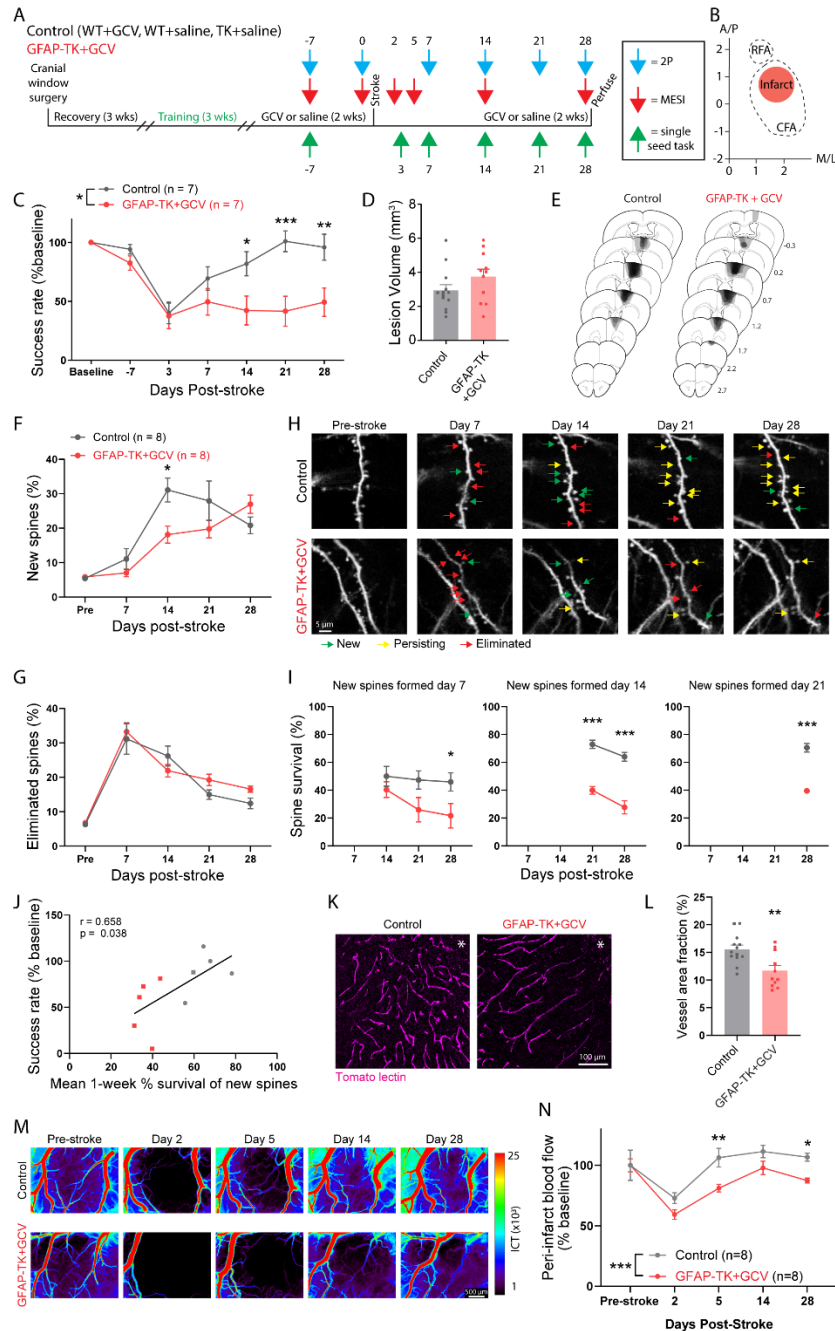
Figure 4. SVZ cytogenesis supports neuronal and vascular remodeling.

A) Experimental design for longitudinal imaging and behavioral testing. Subgroups of mice were subjected to longitudinal imaging and behavioral testing (n = 5/group), imaging only (n = 3/group), behavioral testing only (n = 2/group), and neither (histology only; n = 3 control, n = 1 GFAP-TK+GCV). B) Schematic illustrating infarct placement relative to caudal (CFA) and rostral (RFA) forelimb areas in motor cortex. Axes indicate mm relative to Bregma. C) Performance on the single-seed reaching task. GFAP-TK+GCV mice showed significantly worse

17

309   recovery relative to control mice (significant group x time interaction, $F(6, 72) = 4.7$, $p < 0.001$).
310   *$p < 0.05$, **$p < 0.01$, ***$p < 0.001$, Bonferroni tests. D) Lesion volume was not different
311   between groups ($t(22) = 1.5$, $p = 0.159$). E) Lesion reconstructions. Darker shades represent more
312   overlap between animals. F-J) Longitudinal imaging of dendritic spines revealed altered spine
313   dynamics in mice with ablated neural stem cells. F) New spine formation was significantly
314   higher in control mice on day 14 (significant time x group interaction, $F(4,52) = 4.1$, $p = 0.006$).
315   *$p < 0.05$, Sidak's multiple comparison tests between groups for each day. G) Spine elimination
316   was not significantly different between groups (group effect, $F(1, 66) = 1.2$, $p = 0.285$). H)
317   Longitudinal 2-photon images of GFP-expressing dendritic spines illustrating spine formation
318   (green arrows), persistence of new spines (yellow arrows), and spine elimination (red arrows). I)
319   Survival of new spines was significantly reduced in GFAP-TK+GCV mice. Plots show survival
320   of new spines formed on days 7, 14, and 21 after stroke. *$p < 0.05$, ***$p < 0.001$, Sidak's
321   multiple comparison tests. J) Spine survival was significantly positively correlated with
322   behavioral performance on the final day of testing. K) Representative images of peri-infarct
323   vasculature. L) Peri-infarct vessel density was significantly reduced in GFAP-TK+GCV mice
324   (**$t(22) = 3.3$, $p = 0.004$). M) Representative MESI images of blood flow. N) Peri-infarct blood
325   flow was significantly reduced on days 5 and 28 in GFAP-TK+GCV mice (group effect, $F(1, 14)$
326    $= 32.98$, $p < 0.001$). *$p < 0.05$, **$p < 0.01$, Sidak's multiple comparison tests. Data are presented
327   as mean $\pm$ SEM. Where individual datapoints are shown, datapoints representing males are
328   shown as circles; datapoints representing females are shown as squares.

329

330   *SVZ-derived cells interact with vasculature and produce trophic factors*

331   Neuroblasts originating in the SVZ migrate along vascular scaffolds towards the

332   olfactory bulb in the healthy brain (Bovetti et al., 2007) and towards peri-infarct regions after

333   stroke (Ohab et al., 2006; Thored et al., 2007). We observed frequent contact between lineage-

334   traced SVZ progeny and blood vessels in peri-infarct cortex, including contact of nearby vessels

335   by the processes or cell bodies of 88.2% of SVZ-derived cells (Figure 5A-C). Thus, contact with

336   blood vessels may underlie some of the reparative effects of SVZ-derived cells. In addition,

337   stroke may induce expression of migratory cues in endothelial cells to drive migration of

338   reparative cells from the SVZ (Ohab et al., 2006).

339   Transplanted neural precursors of various sources and in diverse disease settings have

340   been reported to express trophic factors, which may be implicated in their therapeutic effects

18

341   (Andres et al., 2011; Bacigaluppi et al., 2009; Drago et al., 2013; Horie et al., 2011; Llorente et

342   al., 2021; Martino and Pluchino, 2006; Roitbak et al., 2011). To prospectively investigate

343   molecular mechanisms underlying the facilitation of post-stroke repair by SVZ cytogenesis, we

344   examined the expression of four trophic factors known to drive neuronal and vascular growth.

345   ~90% of all SVZ-derived lineage traced cells in peri-infarct cortex expressed VEGF, BDNF,

346   GDNF, and FGF2 (Figure 5D-H). We compared relative abundance of each of these proteins in

347   peri-infarct cortex between control and GFAP-TK+GCV mice at 28 days post-stroke to evaluate

348   production of these factors by SVZ-derived cells relative to other cell types. VEGF protein was

349   significantly reduced in GFAP-TK+GCV mice, indicating that SVZ-derived cells are a major

350   source of VEGF (Figure 5I). Notably, among SVZ-derived cells, all lineages except for new

351   neurons produced VEGF (Figure 5J). These findings suggest that SVZ cytogenesis may facilitate

352   neural repair at least in part through production of trophic factors, particularly VEGF.
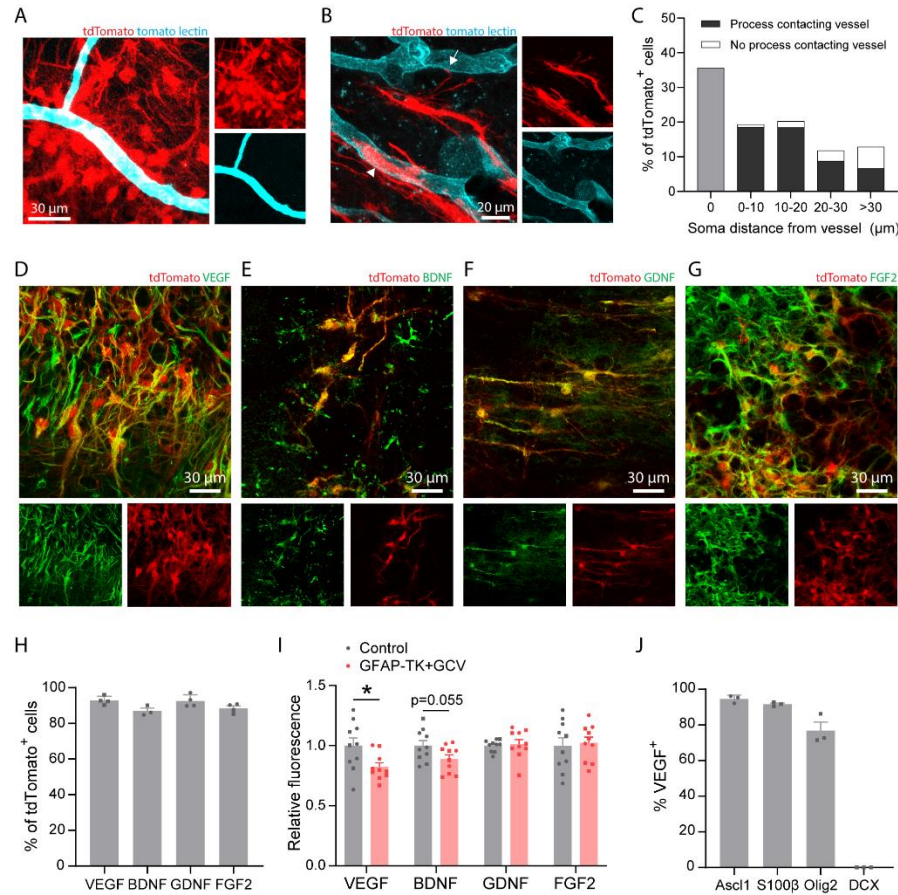
Figure 5. SVZ-derived cells interact with vasculature and produce trophic factors.

A) Confocal image showing clustering of lineage traced cells around blood vessels in peri-infarct cortex. B) tdTomato-expressing cells were frequently observed with cell bodies abutting vessels (arrowhead) or extending processes that terminated on nearby vessels (arrow). C) Quantification of SVZ-derived cell interaction with vasculature in peri-infarct cortex two weeks post-stroke. Data are from 661 cells across 3 Nestin-CreER; Ai14 mice. D-G) Confocal images from peri-infarct cortex showing expression of the trophic factors VEGF (D), BDNF (E), GDNF (F), and FGF2 (G) in tdTomato$^+$ cells. H) Quantification of trophic factor expression in tdTomato$^+$ cells. I) Quantification of trophic factor expression in peri-infarct cortex four weeks post-stroke between control mice and GFAP-TK+GCV mice (n = 10/group). Fluorescence intensity is reported relative to controls. VEGF protein fluorescence was significantly reduced in GFAP-TK+GCV mice. *t(18) = 2.4, p = 0.025. J) Quantification of VEGF expression by phenotype in lineage traced cells. VEGF was expressed by Ascl1$^+$ precursors, S100β$^+$ astrocytes, and Olig2$^+$ oligodendrocyte-lineage cells, but not by neuronal lineage cells (DCX$^+$). Data are presented as mean ± SEM. Where individual datapoints are shown, datapoints representing males are shown as circles; datapoints representing females are shown as squares.
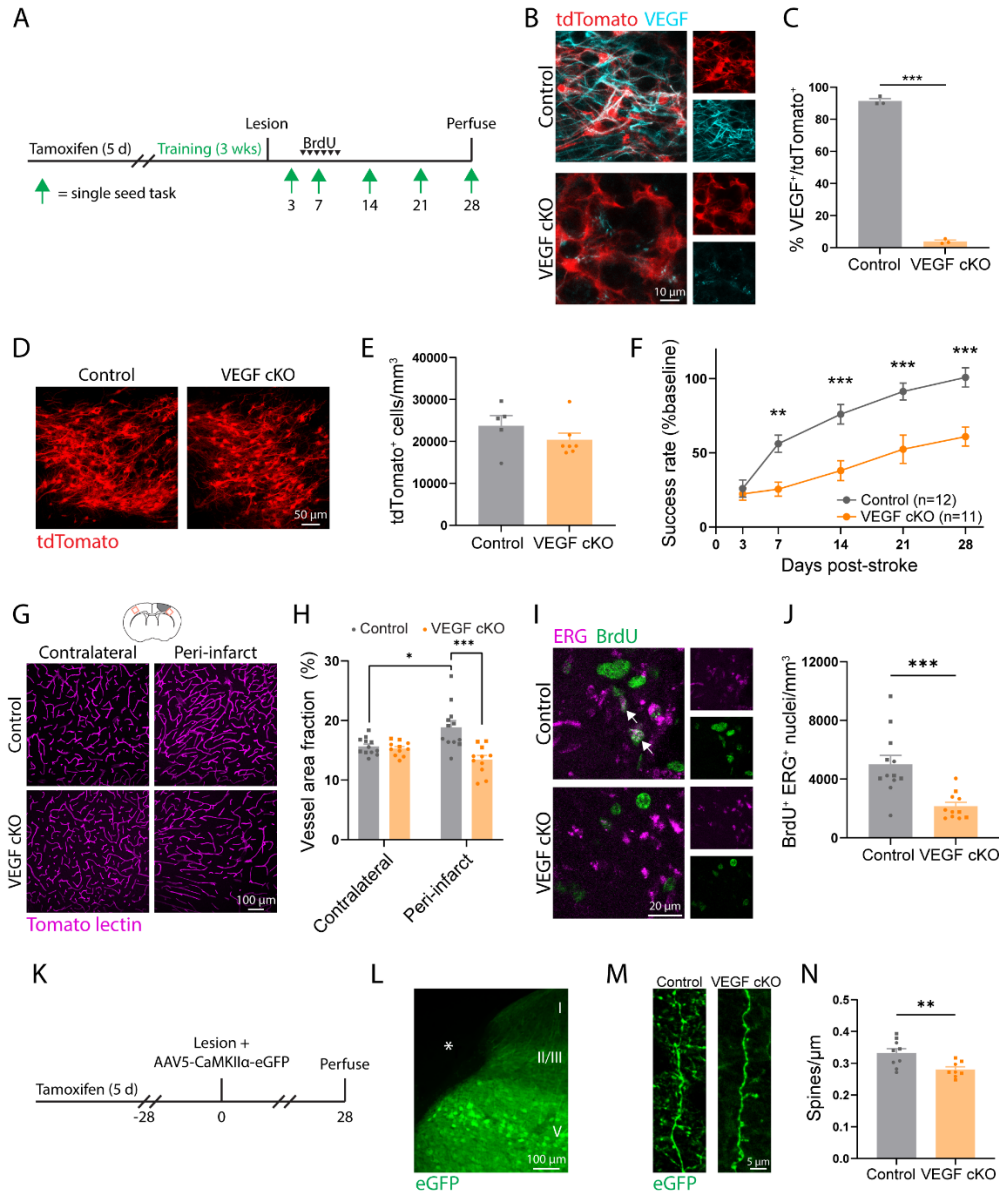
Conditional deletion of Vegf in adult neural stem cells impairs recovery and repair

372   VEGF promotes the growth of blood vessels and neurons (Gerber et al., 1999; Raab et

373 al., 2004; Rosenstein et al., 2003; Sun et al., 2003). We next investigated whether VEGF

374 produced by SVZ-derived cells was involved in post-stroke recovery and repair. We generated

375 *Nestin-CreER*; *Vegf*^fl/fl mice to permit inducible deletion of *Vegf* in adult neural stem cells and

376 their progeny (VEGF cKO; Figure 6A). Lineage tracing in *Nestin-CreER*; *Vegf*^fl/fl; Ai14 mice

377 showed a near complete loss of VEGF in tdTomato$^+$ cells in peri-infarct cortex, but no change in

378 the number of migratory cells relative to controls at two weeks post-stroke (Figure 6B-E).

379 Recovery of forelimb motor function was significantly worse in VEGF cKO mice relative to

380 controls as measured with the single-seed reaching task (Figure 6F). Lesion size and location

381 were not different between groups (Supplemental Figure 5). Vascular remodeling following

382 stroke is seen by increases in peri-infarct vascular density (Williamson et al., 2021, 2020). While

383 vessel density in peri-infarct cortex was increased in control mice relative to the contralateral

384 hemisphere, this was not seen in VEGF cKO mice, and peri-infarct vessel density in VEGF cKO

385 mice was reduced relative to controls (Figure 6G, H). We injected mice with BrdU daily during

386 the peak in angiogenesis from days 5-10 after stroke to quantify new vessel formation. The

387 number of new endothelial cells (BrdU$^+$ERG$^+$) was significantly reduced in VEGF cKO mice,

388 confirming impaired angiogenesis in mice lacking VEGF in SVZ-derived cells.

389   In a separate experiment, we examined the effects of conditional *Vegf* deletion on

390 dendritic spine density after stroke (Figure 6K). Peri-infarct layer V cortical pyramidal neurons

391 were labeled by injections of AAV5-CaMKIIa-eGFP (Figure 6L). Four weeks post-stroke, we

392 quantified spine density on apical dendrites in layer II/III. We previously found that changes in

393 spine density in this region parallel functional recovery (Clark et al., 2019). Spine density was

394 significantly reduced in VEGF cKO mice (Figure 6M, N). Altogether, our results identify VEGF

395   produced by SVZ-derived cells as a key driver of repair and recovery after stroke. More broadly,

396   our findings position newborn cells arising from the SVZ in response to injury as a unique

397   cellular source of trophic support that instructs neural repair.

398

399

Figure 6. Adult neural stem cell-specific deletion of *Vegf* impedes recovery and repair.

401   A) Timeline of experiments to examine recovery in control (Nestin-CreER$^{+/-}$; VEGF$^{fl/+}$, Nestin-
402   CreER$^{-/-}$; VEGF$^{fl/+}$, or Nestin-CreER$^{+/-}$; VEGF$^{+/+}$) and VEGF cKO (Nestin-CreER$^{+/-}$; VEGF$^{fl/fl}$)

22

403   mice. B) Confocal images demonstrating VEGF loss in tdTomato$^+$ cells in Nestin-CreER$^{+/-}$;

404   VEGF$^{fl/fl}$; Ai14 mice. Images are from peri-infarct cortex two weeks post-stroke. C)

405   Substantially fewer tdTomato$^+$ cells express VEGF in VEGF cKO mice. n = 3 mice/group.

406   ***t(4) = 51.23, p < 0.001. D) Representative images of tdTomato$^+$ cells in peri-infarct cortex

407   two weeks post-stroke. (E) There was no difference in peri-infarct tdTomato$^+$ cell density

408   between controls and VEGF cKO mice, indicating that the cytogenic response was unaffected. n

409   = 5 controls, n = 7 VEGF cKO. t(10) = 1.18, p = 0.266. F) VEGF cKO significantly impaired

410   motor recovery measured with the single-seed reaching task (n= 12 control, n = 11 VEGF cKO).

411   Time x group interaction F(4, 84) = 9.2, p < 0.001. **p < 0.01, ***p < 0.001, Sidak's tests

412   between group for each timepoint. G) Representative confocal images and quantification (H) of

413   vasculature show that VEGF cKO markedly reduced peri-infarct vessel density relative to

414   control mice. ***t(21) = 4.1, p < 0.001. Within control mice, peri-infarct vessel density was

415   significantly greater than in contralateral cortex, consistent with stroke-induced

416   neovascularization. *t(22) = 2.8, p = 0.011. By contrast, VEGF cKO mice had diminished vessel

417   density in peri-infarct cortex relative to the intact contralateral cortex, indicating a failure of

418   neovascularization (t(20) = 2.3, p = 0.030). I) Representative confocal images of new endothelial

419   cells (BrdU$^+$ ERG$^+$) in peri-infarct cortex. J) The number of BrdU$^+$ ERG$^+$ nuclei was

420   significantly less in VEGF cKO mice. ***t(15.0) = 4.2, p < 0.001, Welch's corrected t-test. K)

421   Timeline of experiments for evaluating peri-infarct spine density in control (n =9) and VEGF

422   cKO (n = 8) mice. L) Layer V pyramidal neurons were labeled by intracortical injections of

423   AAV5-CaMKiiα-eGFP. Image shows eGFP labeling in peri-infarct cortex. Asterisk indicates

424   lesion core. M) Representative images and quantification (N) of dendritic spine density. Spine

425   density was significantly lower in VEGF cKO mice. **t(15) = 3.0, p = 0.009. Apical dendrites

426   were sampled from layer II/III between 100-700 μm from the infarct border. 2631 spines were

427   counted along 7.9 mm total length of dendrite in controls. 1934 spines were counted along 6.9

428   mm total length of dendrite in cKO mice. Data are presented as mean ± SEM. Where individual

429   datapoints are shown, datapoints representing males are shown as circles; datapoints representing

430   females are shown as squares.

431

432   *AAV-mediated expression of VEGF in peri-infarct cortex enhances recovery in mice with*

433   *arrested cytogenesis*

434   We next tested whether replacement of VEGF would be sufficient to enhance recovery in

435   mice in which cytogenesis was arrested. GFAP-TK mice were trained on the single-seed

436   reaching task and administered GCV to ablate neural stem cells. Immediately after stroke, mice

437   were injected with either AAV5-EF1α-VEGF-P2A-eGFP (AAV-VEGF-eGFP), to induce VEGF

438   and eGFP expression, or AAV5-EF1α-eGFP (AAV-eGFP), to induce only eGFP expression, into

23

439   layer V of peri-infarct cortex (Figure 7A-C). AAV-VEGF-eGFP induced rapid and sustained

440   motor recovery as measured by the single-seed reaching task, whereas AAV-eGFP injected mice

441   showed little improvement up to four weeks post-stroke (Figure 7D). Lesion size and location

442   were not different between groups (Supplemental Figure 6). We examined vascular density in

443   homotopic contralateral and peri-infarct cortex 28 days post-stroke. Vascular density was

444   significantly greater in peri-infarct cortex of AAV-VEGF-eGFP injected mice relative to AAV-

445   eGFP mice (Figure 7E, F). Moreover, there was no difference in vascular density between

446   contralateral and peri-infarct cortex in the AAV-eGFP group, indicating a failure of

447   neovascularization (t(22) = 0.97, p = 0.344). Mice were given daily injections of BrdU during

448   days 5-10 post-stroke to label new blood vessels. AAV-VEGF-eGFP mice had substantially

449   more angiogenesis in peri-infarct cortex than AAV-eGFP mice as measured by the number of

450   BrdU$^+$ERG$^+$ nuclei (Figure 7G, H). Finally, we examined spine density of eGFP-expressing

451   pyramidal neurons on apical dendrites in layer II/III. Spine density was significantly higher in

452   mice given AAV-VEGF-eGFP (Figure 7I, J). In wildtype mice subjected to a sham stroke

453   procedure, AAV-VEGF-eGFP increased vessel density but did not affect motor function

454   (Supplemental Figure 7). Overall, our findings indicate that replacement of VEGF is sufficient to

455   enhance repair and recovery in mice lacking cytogenesis. More broadly, these findings suggest

456   that replacement of factors produced by SVZ-derived cells may constitute an effective therapy.

457
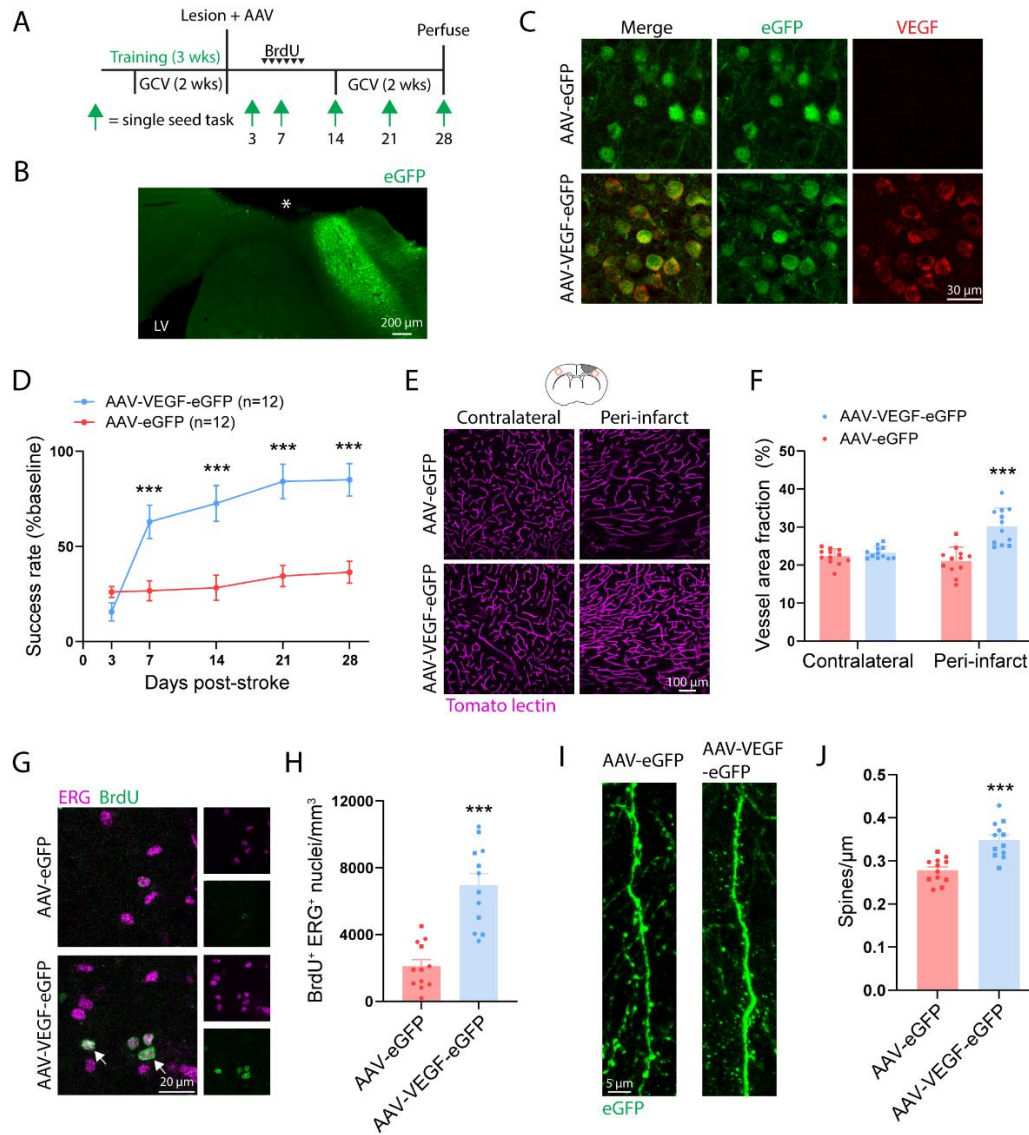
Figure 7. VEGF rescues poor recovery due to neural stem cell ablation.

A) Experimental timeline. Both groups used GFAP-TK mice given GCV to ablate neural stem cells (n = 12 mice per group). Animals were injected with either AAV5-Ef1α-eGFP (AAV-eGFP) or AAV5-Ef1α-VEGF-P2A-eGFP (AAV-VEGF-eGFP) in layer V of peri-infarct cortex. B) Image illustrating AAV targeting of peri-infarct cortex. Asterisk indicates lesion core. LV, lateral ventricle. C) Confocal images validating that AAV-VEGF-eGFP induces VEGF expression. D) AAV-VEGF-eGFP improved motor recovery on the single seed reaching task. Significant time x group interaction $F_{(4, 88)} = 15.9$, $p < 0.001$. $**p < 0.01$, $***p < 0.001$, Sidak's multiple comparison tests. E) Representative confocal images and quantification (F) of vasculature show that AAV-VEGF-eGFP increased peri-infarct vessel density relative to AAV-eGFP mice. $***t_{(22)} = 5.3$, $p < 0.001$, t test. G) Representative confocal images of new endothelial cells (BrdU$^+$ ERG$^+$, arrows) in peri-infarct cortex. H) The number of BrdU$^+$ ERG$^+$

25

470   nuclei was significantly greater in AAV-VEGF-eGFP mice. ***$t(22) = 6.0$, $p < 0.001$. I)

471   Representative images and quantification (J) of dendritic spine density. Spine density was

472   significantly higher in AAV-VEGF-eGFP mice. ***$t(22) = 4.8$, $p < 0.001$. Apical dendrites were

473   sampled from layer II/III between 100-800 μm from the infarct border. 2825 spines were counted

474   along 10.2 mm total length of dendrite in AAV-eGFP mice. 3231 spines were counted along 9.3

475   mm total length of dendrite in AAV-VEGF-eGFP mice. Data are presented as mean ± SEM.

476   Where individual datapoints are shown, datapoints representing males are shown as circles;

477   datapoints representing females are shown as squares.

Discussion

478

479   Our study revealed that a previously underappreciated class of cells, undifferentiated

480   precursors, constitutes the majority of cells that arise from the SVZ and migrate towards the site

481   of injury following stroke. The migration of primarily undifferentiated cells towards the site of

482   injury suggests that the main function of post-injury cytogenesis is likely not cell replacement.

483   We found that reducing SVZ cytogenesis, by neural stem cell ablation or aging, leads to poor

484   functional recovery. Moreover, synaptic and vascular repair were disrupted in mice with

485   deficient cytogenesis. SVZ-derived cells produced trophic factors, most notably VEGF. Loss-of-

486   function experiments demonstrated that VEGF produced by SVZ-derived cells is crucial for

487   effective repair and recovery. Finally, gain-of-function experiments showed that replacement of

488   VEGF was sufficient to enhance recovery in mice lacking cytogenesis. We conclude that trophic

489   support from SVZ-derived cells drives neural repair and functional recovery after stroke. Thus,

490   newborn cells formed in response to injury enable recovery by acting as a unique source of

491   trophic cues that instruct neural repair.

492   With lineage tracing of adult neural stem cells and extensive phenotyping, we identified

493   undifferentiated precursors as the largest subpopulation of SVZ-derived cells after stroke.

494   Undifferentiated neural precursor cells may the better suited than differentiated neural cell types

495   to facilitate neural repair. In culture, neural precursors secrete factors that facilitate vessel

496   formation and neuronal outgrowth (Kirby et al., 2015; Roitbak et al., 2011; Rosenstein et al.,

497   2003). In addition, transplantation of neural stem cells enhances repair and recovery in models of

498   stroke without differentiation of transplanted cells (Andres et al., 2011; Bacigaluppi et al., 2016;

499   Horie et al., 2011; Llorente et al., 2021; Roitbak et al., 2011). Collectively, these studies

500   illustrate the reparative abilities of undifferentiated precursors and suggest that post-stroke

501   cytogenesis facilitates neural repair without substantial cell replacement.

502   Further work is needed to understand how the fate of individual cells is decided among

503   the total population of newborn cells arising from the SVZ. Principles of neural development

504   may apply to cell fate decisions during post-injury cytogenesis in adulthood. For example, the

505   transcription factor NFIA controls gliogenesis during development (Deneen et al., 2006), and is

506   also necessary for SVZ astrogenesis after stroke (Laug et al., 2019). In addition, NFIA inhibits

507   neurogenesis via Notch effectors (David-Bercholz et al., 2021; Deneen et al., 2006).

508   Accordingly, interfering with Notch signalling in neural stem cells biases SVZ progeny towards

509   a neuronal fate and away from an astrocytic fate after stroke (Benner et al., 2013). Additional

510   work will be needed to clarify the mechanisms that dictate phenotypes of SVZ cells responding

511   to stroke, and whether different cell types have distinct reparative functions.

512   Our finding that aging reduces SVZ cytogenesis could be translationally relevant given

513   that stroke incidence increases with age (Kissela et al., 2012). We observed the loss of stroke-

514   induced SVZ proliferation and precursor cell pool expansion in aged mice, which suggests

515   deficient activation of neural precursor cells with aging. Inflammatory signals have been

516   implicated in controlling quiescence/activation of precursors. Chronic inflammatory signals,

517   including interferons, promote stem cell quiescence in aging (Kalamakis et al., 2019). By

518   contrast, acute interferon signaling after stroke stimulates precursor activation (Belenguer et al.,

519   2021; Llorens-Bobadilla et al., 2015). Therefore, inflammatory signaling pathways may be a

520   target to restore cytogenesis in aged animals. We also observed a reduction in the number of

521   cells localized in peri-infarct regions in aged mice that was disproportionate relative to the

522   diminishment of SVZ cytogenesis. Thus, there may also be an age-dependent reduction in either

523   the migratory ability of SVZ cells or the expression of migratory cues at the site of injury.

524   SVZ-derived cells interacted closely with peri-infarct blood vessels and produced trophic

525   factors to facilitate their growth after stroke. The ectopic migration of cells from the SVZ is

526   caused in part by expression of migratory cues in peri-infarct vasculature after stroke (Ohab et

527   al., 2006; Thored et al., 2007). This may be an adaptive response to attract precursors that

528   facilitate tissue growth and repair. Similar processes are mirrored in at least two cases during

529   development. First, neuroepithelial cells produce VEGF to stimulate initial embryonic brain

530   angiogenesis (Breier et al., 1992; Raab et al., 2004). Second, endothelial cues drive

531   oligodendrocyte precursor cell attachment and migration along vessels in the embryonic nervous

532   system (Tsai et al., 2016), and oligodendrocyte precursor-derived HIF-dependent factors,

533   including VEGF, subsequently drive early postnatal angiogenesis (Yuen et al., 2014; Zhang et

534   al., 2020). The ectopic migration of reparative SVZ cells towards injury may represent a reuse of

535   tissue growth mechanisms from development.

536   We have demonstrated that the SVZ cytogenic response to stroke primarily produces

537   undifferentiated precursors that localize to peri-infarct regions – the site of neural repair. SVZ-

538   derived cells produce VEGF that is critical for effective vascular and synaptic plasticity, and

539   ultimately behavioral recovery. Thus, our findings position SVZ cytogenesis as a mechanism that

540   promotes recovery via trophic support rather than cell replacement. These findings provide

541   insight into a fundamental brain repair process and may be relevant for informing treatment

542   strategies.

543   **Materials and Methods**

544   *Subjects and experimental design*

545   Young adult (3-6 months) and aged (12-16 months) mice of both sexes were used. All

546   mice were on a predominantly C57BL/6 background. Transgenic strains were Rosa-CAG-LSL-

547   tdTomato (Ai14, JAX #007914), Nestin-CreER (JAX #016261), ASCL1-CreER (JAX #012882),

548   Rosa-CAG-LSL-Sun1-sfGFP (JAX #021039), GFAP-TK (JAX #005698), Thy1-GFP M-line

549   (JAX #007788), floxed Vegfa (Genentech) (Gerber et al., 1999) (Supplemental Table 1). Mice

550   were bred locally. Animals were housed 2-5 per cage with free access to food and water, except

551   during periods of restricted feeding for behavioral training and assessment. Animals were

552   randomized to groups except when group assignment was dependent on genotype.

553   Experimentation and analysis were done blinded to group allocation. Experiments consisted of 1-

554   5 cohorts of animals. Sample sizes were based on past work using similar methods (Benner et al.,

555   2013; Brown et al., 2007; Clark et al., 2019; Williamson et al., 2021, 2020).

556

557   *Drug administration*

558   100 mg/kg of 20 mg/mL tamoxifen dissolved in corn oil was given (i.p.) daily for 5 consecutive

559   days. 100 mg/kg of 10 mg/mL BrdU dissolved in saline was given (i.p.) once or twice per day

560   for 2 or 6 consecutive days. Ganciclovir dissolved in saline was delivered continuously for 14

561   days via subcutaneous osmotic pumps (Azlet) at a rate of 6.25 µg/hr. In some experiments, a

562   second course of ganciclovir was given beginning two weeks after stroke to maintain stem cell

563   ablation.

564

Cranial window implantation

566   Chronic glass cranial windows were placed over forelimb motor cortex (Clark et al.,

567   2019; Williamson et al., 2021, 2020). Isoflurane (3% induction, 1-2% maintenance) in oxygen

568   was used for anesthesia. Circular craniotomies (~4.5 mm diameter) were made 1.5 mm lateral

569   from Bregma. 4 mm glass windows (Warner Instruments) were secured in place with

570   cyanoacrylate, and exposed skull was covered with dental cement. Carprofen (5 mg/kg, i.p.) was

571   given daily for 7 days to minimize inflammation.

572

Ischemic stroke

574   To model stroke, unilateral photothrombotic lesions were induced in the forelimb region

575   of motor cortex (Tennant et al., 2011; Williamson et al., 2021). Isoflurane (3% induction, 1-2%

576   maintenance) in oxygen was used for anesthesia. Body temperature was maintained with a heated

577   pad for the duration of anesthesia. Stroke was induced through the intact skill by making a scalp

578   incision, administering rose bengal (0.15 mL, 15 mg/mL, i.p.), and illuminating the skull 2 mm

579   lateral from Bregma with a surgical lamp (Schott KL 200) for 15 minutes though a 3 mm

580   aperture. For animals with cranial windows, penetrating arterioles supplying motor cortex were

581   identified by live speckle contrast imaging, and subsequently targeted with a 20 mW 532 nm

582   laser for 15 minutes after administering rose Bengal (0.2 mL, 15 mg/mL, i.p.) (Williamson et al.,

583   2020). Sham stroke procedures involved omitting either illumination or rose bengal.

584

585   *Virus injections*

586   Cortical layer V was targeted for virus injections with a Drummond Nanoject II

587   microinjector through a pulled pipette. Injections were made 0.7 mm below the pial surface at

588   three locations relative to Bregma: 2 mm anterior, 2 mm lateral; 0.5 mm anterior, 3.2 mm lateral;

589   and 1 mm posterior, 2.8 mm lateral. 230 nL was injected per site at a rate of 46 nL/min. The

590   pipette was left in place for 2 minutes after the final injection at each site before it was slowly

591   removed. See Supplemental Table 1 for details on viruses.

592

593   *2-photon imaging of dendritic spines*

594   Mice were anesthetized with isoflurane (3% induction, ~1.5% maintenance) in oxygen

595   and head-fixed to minimize breathing artifacts. Imaging was done with a Prairie Ultima 2-photon

596   microscope with a Ti:Sapphire laser (MaiTai, Spectra Physics) tuned to 870 nm. Image stacks

597   were acquired with 512 x 512 pixel resolution and 0.7 µm z step size using a water-immersion

598   20×/1.0 (Olympus) objective. 4x magnification yielded a 117.2 µm x 117.2 µm field of view.

599   Imaging was done weekly, including two pre-stroke and four post-stroke imaging

600   sessions. During pre-stroke imaging, typically 6-10 regions of unobstructed dendrites were

601   imaged to a depth of ~150 µm. Regions were selected based on a predicted proximity of <1 mm

602   from the infarct. After stroke, the infarct border was identified from blood flow maps and loss of

603   GFP fluorescence (Supplemental Figure 4). Regions within 700 µm of the infarct border were re-

604   imaged at subsequent time points in order to track spine dynamics during recovery. In some

605   animals, additional imaging regions were added after stroke. Time lapse images of dendrites >30

606   µm in length with clearly visible spines were analyzed to quantify spine formation and

607   elimination, and persistence of newly formed spines (Clark et al., 2019; Joy et al., 2019; Tennant

608   et al., 2017).

609

610   *Blood flow imaging*

611   Blood flow was imaged through cranial windows with multi-exposure speckle imaging, a

612   label-free, quantitative, optical method (Clark et al., 2019; Williamson et al., 2021, 2020).

613   Anesthetic level was consistent across all imaging sessions (1.25% isoflurane in oxygen). Two

614   pre-stroke images were collected to establish baseline blood flow. Post-stroke images were

615   collected on days 2, 5, 14, and 28. Each imaging session lasted <10 mins. Blood flow was

616   measured in parenchymal regions and tracked over time as before (Williamson et al., 2021).

617

618   *Behavioral testing*

619   Skilled forelimb use was assessed with the single seed reaching task, which is highly

620   sensitive to deficits caused by motor cortical damage and is translationally relevant (Clark et al.,

621   2019; Klein et al., 2012; van Lieshout et al., 2021; Williamson et al., 2020). Animals were food

622   restricted to ~90% free feeding weight to encourage reaching. First, animals were shaped on the

623   task and the preferred paw for reaching was determined over 2-5 days. Training was done over

624   15 sessions, once per day, five days per week. Each session consisted of 30 trials. For each trial,

625   animals were allowed up to two reach attempts. A successful reach was defined as the animal

626   grasping the seed and bringing it to its mouth. Failure was defined as missing the seed, knocking

627   it out of the well, or releasing it before it was brought to the animal's mouth. Baseline

33

628 performance was defined as the mean success rate per trial over the last three training sessions.

629 Inclusion criteria was a minimum baseline success rate of 30%. 1 mouse (GFAP-TK+GCV) from

630 the experiment in Figure 2,8 mice (n = 7 control, n = 1 GFAP-TK+GCV) from the experiment in

631 Figure 3, and 2 mice (n = 1 AAV-eGFP, n = 1 AAV-VEGF-eGFP) from the experiment in

632 Supplemental Figure 7 failed to meet this threshold and were excluded. Test sessions were done

633 on days 3, 7, 14, 21, and 28 post-stroke.

634

635 *Histology and image analysis*

636 Mice were euthanized by overdosed with a pentobarbitol/phenytoin solution followed by

637 perfusion with 0.1M phosphate buffer and 4% paraformaldehyde in phosphate buffer. Brains

638 were postfixed overnight at 4°C. 35 µm coronal sections were collected with a vibratome

639 (VT1000S, Leica). To label vasculature, mice were retro-orbitally injected with 0.1 mL of

640 Dylight 594- or 649-conjuagated tomato lectin 5 minutes prior to perfusion (Williamson et al.,

641 2021, 2020). To examine vascular permeability, mice were retro-orbitally injected with 0.1 mL

642 of 50 mg/mL FITC-conjugated albumin 2 hours prior to perfusion.

643 To create lesion reconstructions and quantify lesion volume, one set of every fifth section

644 was Nissl stained. Lesions were reconstructed as previously described (Kim et al., 2018). Lesion

645 volume was calculated using Cavalieri's method as the difference in volume between uninjured

646 and injured cortex.

647 Immunohistochemical staining was done by washing tissue in phosphate buffered saline

648 (PBS), blocking with 10% donkey serum in PBS with 0.25% Triton for 60 minutes, incubating

649 with primary antibodies overnight (antibodies and dilutions are reported in Supplemental Table

34

650 1), washing in PBS, incubating with species appropriate 405-, 488-, 594, or 647-conjugated

651 secondary antibodies, and washing a final time in PBS. Tissue was pretreated with 2 N HCl (30

652 mins) followed by 0.1 M boric acid (10 mins) when staining for BrdU.

653 Confocal images with 1-2 µm Z-step size were collected with a Leica TCS SP5

654 microscope. 20×/0.7 NA and 40×/1.0NA objectives were used. Acquisition settings were

655 consistent between samples. Typically, 3 sections were imaged per region of interest per mouse.

656 FIJI was used for image analysis. Area fraction and fluorescence intensity were

657 quantified as before (Williamson et al., 2021). The optical disector method was used to count cell

658 density. Cell density was calculated by number of cells / (frame area × section thickness).

659

660 *Statistics*

661 Data are expressed as mean ± S.E.M. Measurements from individual animals are shown on plots

662 as datapoints where possible. Data were analyzed with GraphPad Prism version 9.3. Independent

663 samples were compared with two-tailed t tests. Variance was assessed with F tests, and Welch's

664 corrected t tests were used in cases where variance was significantly different. One- and two-way

665 ANOVAs, mixed-effects analyses, and linear regressions were used as noted in the text. Post hoc

666 tests were used following significant ANOVA as noted in the text. Details on the statistical tests

667 used for each experiment are located in the Results and figure legends. Alpha was set at $P < 0.05$.

668

669 *Study approval*

670   Animal use was in accordance with a protocol approved by the Institutional Animal Care and

671   Use Committee at the University of Texas at Austin.

Author contributions

673   Conceptualization: M.R.W.; Methodology: M.R.W., T.A.J., and M.R.D.; Investigation and

674   analysis: M.R.W., S.P.L., R.L.F., N.A.D., and J.L.R.; Writing – Original Draft: M.R.W.; Writing

675   – Review & Editing: all authors; Supervision: T.A.J. and M.R.D.; Funding Acquisition: A.K.D.,

676   M.R.D., and T.A.J.

677

685

Competing Interests

687   None.

688   **References**

689   Andres RH, Horie N, Slikker W, Keren-gill H, Zhan K, Sun G, Manley NC, Pereira MP, Sheikh

690   LA, Mcmillan EL, Schaar BT, Svendsen CN, Bliss TM, Steinberg GK. 2011. Human neural

691   stem cells enhance structural plasticity and axonal transport in the ischaemic brain. *Brain*

692   **134**:1777–1780. doi:10.1093/brain/awr094

693   Arvidsson A, Collin T, Kirik D, Kokaia Z, Lindvall O. 2002. Neuronal replacement from

694   endogenous precursors in the adult brain after stroke. *Nat Med* **8**:963–970.

695   doi:10.1038/nm747

696   Bacigaluppi M, Pluchino S, Jametti LP, Kilic E, Salani G, Brambilla E, West MJ, Comi G. 2009.

697   Delayed post-ischaemic neuroprotection following systemic neural stem cell transplantation

698   involves multiple mechanisms. *Brain* **132**:2239–2251. doi:10.1093/brain/awp174

699   Bacigaluppi M, Russo GL, Peruzzotti-Jametti L, Rossi S, Sandrone S, Butti E, Ceglia R De,

700   Bergamaschi A, Motta C, Gallizioli M, Studer V, Colombo E, Farina C, Comi G, Politi LS,

701   Muzio L, Villani C, Invernizzi RW, Hermann DM, Centonze D, Martino G. 2016. Neural

702   Stem Cell Transplantation Induces Stroke Recovery by Upregulating Glutamate Transporter

703   GLT-1 in Astrocytes. *J Neurosci* **36**:10529–10544. doi:10.1523/JNEUROSCI.1643-16.2016

704   Belenguer G, Duart-Abadia P, Jordan-Pla A, Domingo-Muelas A, Blasco-Chamarro L, Ferron

705   SR, Morante-Redolat JM, Farinas I. 2021. Adult Neural Stem Cells Are Alerted by

706   Systemic Inflammation through TNF-a Receptor Signaling. *Cell Stem Cell* **28**:285–299.

707   doi:10.1016/j.stem.2020.10.016

708   Benner EJ, Luciano D, Jo R, Abdi K, Paez-Gonzalez P, Sheng H, Warner D, Liu C, Eroglu C,

709   Kuo CT. 2013. Post-injury protective astrogenesis from SVZ niche is controlled by Notch

710   modulator Thbs4. *Nature* **497**:369–373. doi:10.1038/nature12069.Post-injury

711   Bouab M, Paliouras GN, Aumont A, Berard-Forest K, Fernandes KJL. 2011. Aging of the

712   Subventricular Zone Neural Stem Cell Niche: Evidence for Quiescence-Associated Changes

713   Between Early and Mid-Adulthood. *Neuroscience* **173**:135–149.

714   doi:10.1016/j.neuroscience.2010.11.032

715   Bovetti S, Hsieh Y, Bovolin P, Perroteau I, Kazunori T, Puche AC. 2007. Blood Vessels Form a

716   Scaffold for Neuroblast Migration in the Adult Olfactory Bulb. *J Neurosci* **27**:5976–5980.

717   doi:10.1523/JNEUROSCI.0678-07.2007

718   Breier G, Albrecht U, Sterrer S, Risau W. 1992. Expression of vascular endothelial growth factor

719   during embryonic angiogenesis and endothelial cell differentiation. *Development* **114**:521–

720   532. doi:10.1242/dev.114.2.521

721   Brown CE, Li P, Boyd JD, Delaney KR, Murphy TH. 2007. Extensive Turnover of Dendritic

722   Spines and Vascular Remodeling in Cortical Tissues Recovering from Stroke. *J Neurosci*

723   **27**:4101–4109. doi:10.1523/JNEUROSCI.4295-06.2007

724   Clark TA, Sullender C, Jacob D, Zuo Y, Dunn AK, Jones TA. 2019. Rehabilitative Training

725   Interacts with Ischemia-Instigated Spine Dynamics to Promote a Lasting Population of New

726   Synapses in Peri-Infarct Motor Cortex. *J Neurosci* **39**:8471–8483.

727   doi:10.1523/JNEUROSCI.1141-19.2019

728   Codega P, Silva-vargas V, Paul A, Maldonado-soto AR, Deleo AM, Pastrana E. 2014.

729   Prospective Identification and Purification of Quiescent Adult Neural Stem Cells from

730   Their In Vivo Niche. *Neuron* **82**:545–559. doi:10.1016/j.neuron.2014.02.039

731   David-Bercholz J, Kuo CT, Deneen B. 2021. Astrocyte and Oligodendrocyte Responses From

732   the Subventricular Zone After Injury. *Front Cell Neurosci* **15**:797553.

733   doi:10.3389/fncel.2021.797553

734   Deneen B, Ho R, Lukaszewicz A, Hochstim CJ, Gronostajski RM, Anderson DJ. 2006. The

735   Transcription Factor NFIA Controls the Onset of Gliogenesis in the Developing Spinal

736   Cord. *Neuron* **52**:953–968. doi:10.1016/j.neuron.2006.11.019

737   Doetsch F, Caille I, Lim DA, Garcı JM, Alvarez-buylla A. 1999. Subventricular Zone Astrocytes

738   Are Neural Stem Cells in the Adult Mammalian Brain. *Cell* **97**:703–716.

739   Drago D, Cossetti C, Iraci N, Gaude E, Musco G, Bachi A, Pluchino S. 2013. The stem cell

740   secretome and its role in brain repair. *Biochimie* **95**:2271–2285.

741   doi:10.1016/j.biochi.2013.06.020

742   Faiz M, Sachewsky N, Gascon S, Bang KWA, Morshead CM, Nagy A. 2015. Adult Neural Stem

743   Cells from the Subventricular Zone Give Rise to Reactive Astrocytes in the Cortex after

744   Stroke. *Cell Stem Cell* **17**:624–634. doi:10.1016/j.stem.2015.08.002

745   Garcia ADR, Doan NB, Imura T, Bush TG, Sofroniew M V. 2004. GFAP-expressing progenitors

746   are the principal source of constitutive neurogenesis in adult mouse forebrain. *Nat Neurosci*

747   **7**:1233–1241. doi:10.1038/nn1340

748   Gerber HP, Hillan KJ, Ryan AM, Kowalski J, Keller GA, Rangell L, Wright BD, Radtke F,

749   Aguet M, Ferrara N. 1999. VEGF is required for growth and survival in neonatal mice.

750   *Development* **126**:1149–1159.

751 Götz M, Sirko S, Beckers J, Irmler M. 2015. Reactive astrocytes as neural stem or progenitor

752 cells: In vivo lineage, In vitro potential, and Genome-wide expression analysis. *Glia*

753 **63**:1452–1468. doi:10.1002/glia.22850

754 He F, Sullender C, Zhu H, Williamson MR, Li X, Zhao Z, Jones TA, Xie C, Dunn AK, Luan L.

755 2020. Multimodal mapping of neural activity and cerebral blood flow reveals long-lasting

756 neurovascular dissociations after small-scale strokes. *Sci Adv* **6**:eaba1933.

757 doi:10.1101/2020.03.04.977322

758 Horie N, Pereira MP, Niizuma K, Sun G, Keren-Gill H, Encarnacion A, Shamloo M, Hamilton

759 SA, Jiang K, Huhn S, Palmer TD, Bliss TM, Steinberg GK. 2011. Transplanted stem cell-

760 secreted vascular endothelial growth factor effects poststroke recovery, inflammation, and

761 vascular repair. *Stem Cells* **29**:274–285. doi:10.1002/stem.584

762 Jin K, Minami M, Xie L, Sun Y, Mao XO, Wang Y, Simon RP, Greenberg DA. 2004. Ischemia-

763 induced neurogenesis is preserved but reduced in the aged rodent brain. *Aging Cell* **3**:373–

764 377. doi:10.1111/j.1474-9728.2004.00131.x

765 Joy MT, Ben Assayag E, Shabashov-Stone D, Liraz-Zaltsman S, Mazzitelli J, Arenas M,

766 Abduljawad N, Kliper E, Korczyn AD, Thareja NS, Kesner EL, Zhou M, Huang S, Silva

767 TK, Katz N, Bornstein NM, Silva AJ, Shohami E, Carmichael ST. 2019. CCR5 Is a

768 Therapeutic Target for Recovery after Stroke and Traumatic Brain Injury. *Cell* **176**:1143-

769 1157.e13. doi:10.1016/j.cell.2019.01.044

770 Kalamakis G, Brune D, Ravichandran S, Bolz J, Fan W, Ziebell F, Stiehl T, Catala-Martinez F,

771 Kupke J, Zhao S, Llorens-Bobadilla E, Bauer K, Limpert S, Berger B, Christen U,

772 Schmezer P, Mallm JP, Berninger B, Anders S, del Sol A, Marciniak-Czochra A, Martin-

773   Villalba A. 2019. Quiescence Modulates Stem Cell Maintenance and Regenerative Capacity

774   in the Aging Brain. *Cell* **176**:1407–1419. doi:10.1016/j.cell.2019.01.040

775   Kannangara TS, Carter A, Xue Y, Dhaliwal JS, Béïque J-C, Lagace DC. 2018. Excitable Adult-

776   Generated GABAergic Neurons Acquire Functional Innervation in the Cortex after Stroke.

777   *Stem Cell Reports* **11**:1327–1336. doi:10.1016/j.stemcr.2018.10.011

778   Kim SY, Hsu JE, Husbands LC, Kleim JA, Jones TA. 2018. Coordinated Plasticity of Synapses

779   and Astrocytes Underlies Practice-Driven Functional Vicariation in Peri-Infarct Motor

780   Cortex. *J Neurosci* **38**:93–107. doi:10.1523/JNEUROSCI.1295-17.2017

781   Kirby ED, Kuwahara AA, Messer RL, Wyss-Coray T. 2015. Adult hippocampal neural stem and

782   progenitor cells regulate the neurogenic niche by secreting VEGF. *Proc Natl Acad Sci*

783   **112**:4128–4133. doi:10.1073/pnas.1422448112

784   Kissela BM, Khoury JC, Alwell K, Moomaw CJ, Woo D, Adeoye O, Flaherty ML, Ferioli S, De

785   Los Rios La Rosa F, Broderick JP, Kleindorfer DO. 2012. Age at stroke: Temporal trends in

786   stroke incidence in a large, biracial population. *Neurology* **79**:1781–1787.

787   Klein A, Sacrey LAR, Whishaw IQ, Dunnett SB. 2012. The use of rodent skilled reaching as a

788   translational model for investigating brain damage and disease. *Neurosci Biobehav Rev*

789   **36**:1030–1042. doi:10.1016/j.neubiorev.2011.12.010

790   Lagace DC. 2012. Does the endogenous neurogenic response alter behavioral recovery following

791   stroke? *Behav Brain Res* **227**:426–432. doi:10.1016/j.bbr.2011.08.045

792   Lattke M, Goldstone R, Ellis JK, Boeing S, Jurado-Arjona J, Marichal N, MacRae JI, Berninger

793   B, Guillemot F. 2021. Extensive transcriptional and chromatin changes underlie astrocyte

794   maturation in vivo and in culture. *Nat Commun* **12**. doi:10.1038/s41467-021-24624-5

795   Laug D, Huang TW, Bosquez Huerta NA, Huang AYS, Sardar D, Ortiz-Guzman J, Carlson JC,

796   Arenkiel BR, Kuo CT, Mohila CA, Glasgow SM, Lee HK, Deneen B. 2019. Nuclear factor

797   I-A regulates diverse reactive astrocyte responses after CNS injury. *J Clin Invest* **129**:4408–

798   4418. doi:10.1172/JCI127492

799   Li L, Candelario KM, Thomas K, Wang R, Wright K, Messier A, Cunningham LA. 2014.

800   Hypoxia inducible factor-1α (HIF-1α) is required for neural stem cell maintenance and

801   vascular stability in the adult mouse SVZ. *J Neurosci* **34**:16713–16719.

802   doi:10.1523/JNEUROSCI.4590-13.2014

803   Li L, Harms KM, Ventura PB, Lagace DC, Eisch AJ, Cunningham LA. 2010. Focal Cerebral

804   Ischemia Induces a Multilineage Cytogenic Response from Adult Subventricular Zone that

805   is Predominantly Gliogenic. *Glia* **58**:1610–1619. doi:10.1002/glia.21033

806   Liang H, Zhao H, Gleichman A, Machnicki M, Telang S, Tang S, Rshtouni M, Ruddell J,

807   Thomas Carmichael S. 2019. Region-specific and activity-dependent regulation of SVZ

808   neurogenesis and recovery after stroke. *Proc Natl Acad Sci U S A* **116**:13621–13630.

809   doi:10.1073/pnas.1811825116

810   Lin C-CJ, Yu K, Hatcher A, Huang T, Lee HK, Carlson J, Weston MC, Chen F, Zhang Y, Zhu

811   W, Mohila CA, Ahmed N, Patel AJ, Arenkiel BR, Noebels JL, Creighton CJ, Deneen B.

812   2017. Identification of diverse astrocyte populations and their malignant analogs. *Nat*

813   *Neurosci* **20**:396–405. doi:10.1038/nn.4493

814   Llorens-Bobadilla E, Zhao S, Baser A, Saiz-Castro G, Martin-Villalba A. 2015. Single-Cell

815   Transcriptomics Reveals a Population of Dormant Neural Stem Cells that Become

816   Activated upon Brain Injury Article Single-Cell Transcriptomics Reveals a Population of

817   Dormant Neural Stem Cells that Become Activated upon Brain Injury. *Cell Stem Cell*

818   **17**:329–340. doi:10.1016/j.stem.2015.07.002

819   Llorente IL, Xie Y, Mazzitelli JA, Hatanaka EA, Cinkornpumin J, Miller DR, Lin Y, Lowry WE,

820   Carmichael ST. 2021. Patient-derived glial enriched progenitors repair functional deficits

821   due to white matter stroke and vascular dementia in rodents. *Sci Transl Med* **13**:eaaz6747.

822   Luo J, Daniels SB, Lennington JB, Notti RQ, Conover JC. 2006. The aging neurogenic

823   subventricular zone. *Aging Cell* 139–152. doi:10.1111/j.1474-9726.2006.00197.x

824   Magnusson JP, Göritz C, Tatarishvili J, Dias DO, Smith EMK, Lindvall O, Kokaia Z, Frisén J.

825   2014. A latent neurogenic program in astrocytes regulated by Notch signaling in the mouse.

826   *Science (80-)* **346**:237–241. doi:10.1126/science.346.6206.237

827   Martino G, Pluchino S. 2006. The therapeutic potential of neural stem cells. *Nat Rev Neurosci*

828   **7**:395–406.

829   Mostany R, Chowdhury TG, Johnston DG, Portonovo SA, Carmichael ST, Portera-Cailliau C.

830   2010. Local hemodynamics dictate long-term dendritic plasticity in peri-infarct cortex. *J*

831   *Neurosci* **30**:14116–14126. doi:10.1523/JNEUROSCI.3908-10.2010

832   Ohab JJ, Fleming S, Blesch A, Carmichael ST. 2006. A neurovascular niche for neurogenesis

833   after stroke. *J Neurosci* **26**:13007–13016. doi:10.1523/JNEUROSCI.4323-06.2006

834   Paolucci S, Antonucci G, Troisi E, Bragoni M, Coiro P, De Angelis D, Pratesi L, Venturiero V,

835   Grasso MG. 2003. Aging and stroke rehabilitation. a case-comparison study. *Cerebrovasc*

836   *Disord* **15**:98–105.

837   Parent JM, Vexler ZS, Gong C, Derugin N, Ferriero DM. 2002. Rat Forebrain Neurogenesis and

838   Striatal Neuron Replacement after Focal Stroke. *Ann Neurol* **52**:802–813.

839   Pluchino S, Zanotti L, Rossi B, Brambilla E, Ottoboni L, Salani G, Martinello M, Cattalini A,

840   Bergami A, Furlan R, Comi G, Constantin G, Martino G. 2005. Neurosphere-derived

841   multipotent precursors promote neuroprotection by an immunomodulatory mechanism.

842   *Nature* **436**:266–271. doi:10.1038/nature03889

843   Raab S, Beck H, Gaumann A, Yüce A, Gerber HP, Plate K, Hammes H-P, Ferrara N, Breier G.

844   2004. Impaired brain angiogenesis and neuronal apoptosis induced by conditional

845   homozygous inactivation of vascular endothelial growth factor. *Thromb Haemost* **91**:595–

846   605. doi:10.1160/th03-09-0582

847   Raponi E, Agenes F, Delphin C, Assard N, Baudier J, Legraverend C, Deloulme J. 2007. S100B

848   Expression Defines a State in Which GFAP-Expressing Cells Lose Their Neural Stem Cell

849   Potential and Acquire a More Mature Developmental Stage. *Glia* **177**:165–177.

850   doi:10.1002/glia

851   Robel S, Berninger B, Götz M. 2011. The stem cell potential of glia: Lessons from reactive

852   gliosis. *Nat Rev Neurosci*. doi:10.1038/nrn2978

853   Roitbak T, Li L, Cunningham LA. 2011. Neural Stem/Progenitor Cells Promote Endothelial Cell

854   Morphogenesis and Protect Endothelial Cells against Ischemia via HIF-1α-regulated VEGF

855   Signaling. *J Cereb Blood Flow Metab* **28**:1530–1542. doi:10.1038/jcbfm.2008.38.Neural

856   Rosenstein JM, Mani N, Khaibullina A, Krum JM. 2003. Neurotrophic Effects of Vascular

45

857   Endothelial Growth Factor on Organotypic Cortical Explants and Primary Cortical Neurons.

858   *J Neurosci* **23**:11036–11044. doi:10.1523/jneurosci.23-35-11036.2003

859   Sabelström H, Stenudd M, Réu P, Dias DO, Elfineh M, Zdunek S, Damberg P, Göritz C, Frisén

860   J. 2013. Resident Neural Stem Cells Restrict Tissue Damage and Neuronal Loss After

861   Spinal Cord Injury in Mice. *Science (80-)* **537**:534–537.

862   Sun Y, Logvinova A, Greenberg DA, Sun Y, Jin K, Xie L, Childs J, Mao XO, Logvinova A,

863   Greenberg DA. 2003. VEGF-induced neuroprotection, neurogenesis, and angiogenesis after

864   focal cerebral ischemia. *J Clin Invest* **111**:1843–1851.

865   doi:10.1172/JCI200317977.Introduction

866   Swan AA, Clutton JE, Chary PK, Cook SG, Liu GG, Drew MR. 2014. Characterization of the

867   role of adult neurogenesis in touch-screen discrimination learning. *Hippocampus* **24**:1581–

868   1591. doi:10.1002/hipo.22337

869   Tennant KA, Adkins DL, Donlan NA, Asay AL, Thomas N, Kleim JA, Jones TA. 2011. The

870   organization of the forelimb representation of the C57BL/6 mouse motor cortex as defined

871   by intracortical microstimulation and cytoarchitecture. *Cereb Cortex* **21**:865–876.

872   doi:10.1093/cercor/bhq159

873   Tennant KA, Taylor SL, White ER, Brown CE. 2017. Optogenetic rewiring of thalamocortical

874   circuits to restore function in the stroke injured brain. *Nat Commun* **8**:15879.

875   doi:10.1038/ncomms15879

876   Thored P, Wood J, Arvidsson A, Kokaia Z, Lindvall O. 2007. Long-Term Neuroblast Migration

877   Along Blood Vessels in an Area With Transient Angiogenesis and Increased

878   Vascularization after Stroke. *Stroke* **38**:3032–9. doi:10.1161/STROKEAHA.107.488445

879   Tsai HH, Niu J, Munji R, Davalos D, Chang J, Zhang H, Tien AC, Kuo CJ, Chan JR, Daneman

880   R, Fancy SPJ. 2016. Oligodendrocyte precursors migrate along vasculature in the

881   developing nervous system. *Science (80-)* **351**:379–384. doi:10.1126/science.aad3839

882   van Lieshout ECC, Boonzaier J, Pel AJ, van Heijningen CL, Vink JJ, Visser-Meily JMA, van

883   Tilborg GAF, Dijkhuizen RM. 2021. Translational Value of Skilled Reaching Assessment

884   in Clinical and Preclinical Studies on Motor Recovery After Stroke. *Neurorehabil Neural*

885   *Repair* **35**:457–467. doi:10.1177/15459683211005022

886   Williamson MR, Franzen RL, Fuertes CJA, Dunn AK, Drew MR, Jones TA. 2020. A window of

887   vascular plasticity coupled to behavioral recovery after stroke. *J Neurosci* **40**:7651–7667.

888   doi:10.1523/jneurosci.1464-20.2020

889   Williamson MR, Fuertes CJA, Dunn AK, Drew MR, Jones TA. 2021. Reactive astrocytes

890   facilitate vascular repair and remodeling after stroke. *Cell Rep* **35**:109048.

891   doi:10.1016/j.celrep.2021.109048

892   Williamson MR, Jones TA, Drew MR. 2019. Functions of subventricular zone neural precursor

893   cells in stroke recovery. *Behav Brain Res*. doi:10.1016/j.bbr.2019.112209

894   Yuen TJ, Silbereis JC, Griveau A, Chang SM, Daneman R, Fancy SPJ, Zahed H, Maltepe E,

895   Rowitch DH. 2014. Oligodendrocyte-encoded HIF function couples postnatal myelination

896   and white matter angiogenesis. *Cell* **158**:383–396. doi:10.1016/j.cell.2014.04.052

897   Zamboni M, Llorens-Bobadilla E, Magnusson JP, Frisén J. 2020. A Widespread Neurogenic

898   Potential of Neocortical Astrocytes Is Induced by Injury. *Cell Stem Cell* **27**:605-617.e5.
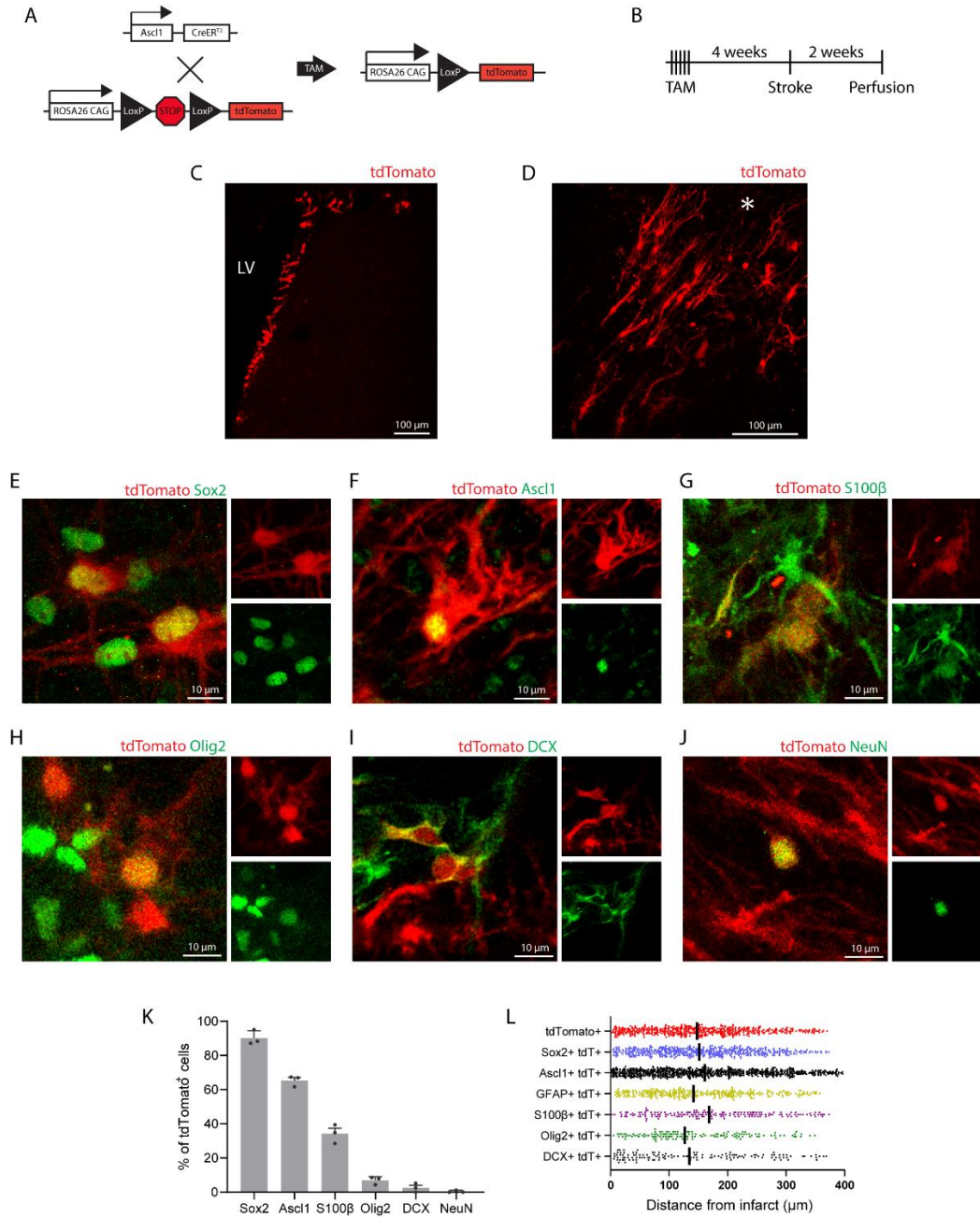
899   doi:10.1016/j.stem.2020.07.006

900   Zhang S, Kim B, Zhu X, Gui X, Wang Y, Lan Z, Prabhu P, Fond K, Wang A, Guo F. 2020. Glial

901   type specific regulation of CNS angiogenesis by HIFα-activated different signaling

902   pathways. *Nat Commun* **11**:2027. doi:10.1038/s41467-020-15656-4

903

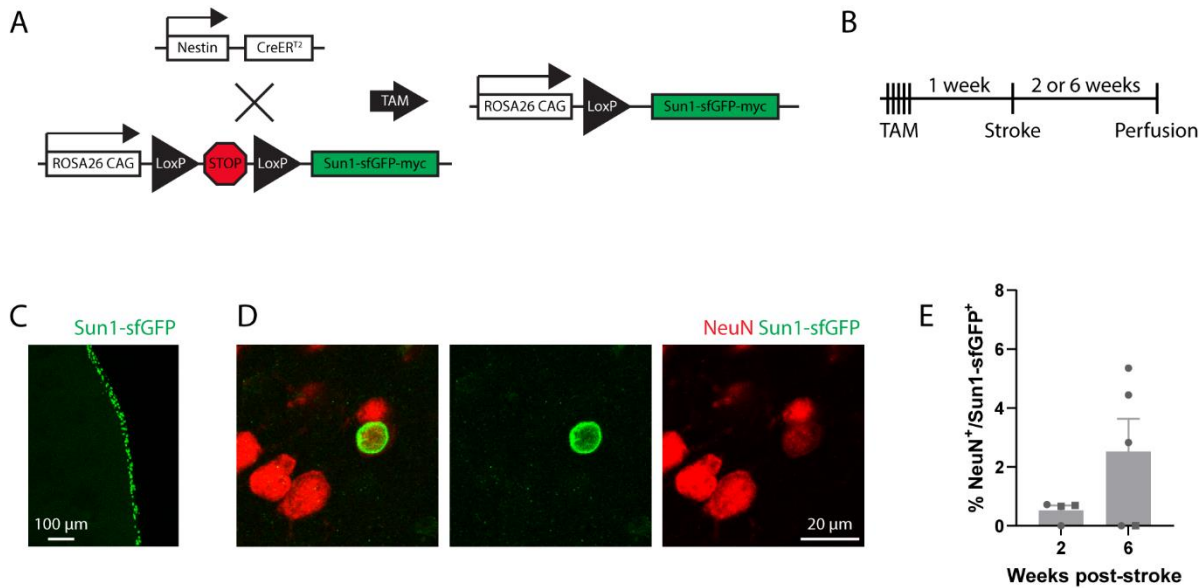904   **Supplemental figures and tables**

905

906

907   **Supplemental Figure 1. SVZ-derived cells are predominantly undifferentiated precursors**

908   **and astrocytes.**

909   A) Schematic of genetic lineage tracing system where tamoxifen (TAM) induces indelible

910   expression of tdTomato in Ascl1-expressing neural stem cells, intermediate progenitor cells, and

911   their progeny. B) Experimental design. C) Image showing tdTomato expression in the SVZ. LV,

912   lateral ventricle. D) Representative image of tdTomato$^+$ cells localized to peri-infarct cortex 2

913   weeks after a cortical stroke (asterisk). E-J) Lineage tracing using Ascl1-CreER; Ai14 mice

914   corroborates the major finding of Figure 1, that SVZ-derived cells in peri-infarct cortex are

915   predominantly undifferentiated precursors and astrocytes. Representative images illustrating co-

916   labeling of lineage traced tdTomato$^+$ cells with differentiation stage-specific markers at two

917   weeks post-stroke (E) Sox2, F) Ascl1, G) S100β, H) Olig2, I) DCX. J) NeuN). K) Quantification

918   of marker expression by % of tdTomato$^+$ cells. Data are presented as mean ± SEM. L) Spatial

919   distribution of cells relative to the infarct border by marker expression at 2 weeks post-stroke in

920   Nestin-CreER; Ai14 mice. Each point indicates a single cell. Vertical lines indicate medians.

921   There was no clear pattern of spatial organization by cell type. Distance was measured as the

922   distance to the nearest part of the infarct border within a given section for each cell. Only cells

923   within 400 µm of the infarct border and within cortex were included in this analysis.

924

925

926

Supplemental Figure 2. Few SVZ-derived cells become neurons.

A) Schematic of genetic lineage tracing system where tamoxifen (TAM) induces indelible

expression of a nuclear membrane-bound Sun1-sfGFP in neural stem cells and their progeny. B)

Experimental design. C) Image showing Sun1-sfGFP expression in the SVZ. D) Representative

image of a NeuN$^+$Sun1-sfGFP$^+$ nucleus in peri-infarct cortex. E) Quantification of SVZ-derived

neurons. Data were derived from a combined 1014 nuclei counted across nine mice (n = 4 at two

weeks, n = 5 at six weeks). There was not a significant difference between time points (t(4.2) =

1.79, p = 0.145, Welch's corrected t test). Data are presented as mean ± SEM. Datapoints

representing males are shown as circles; datapoints representing females are shown as squares.

936

937
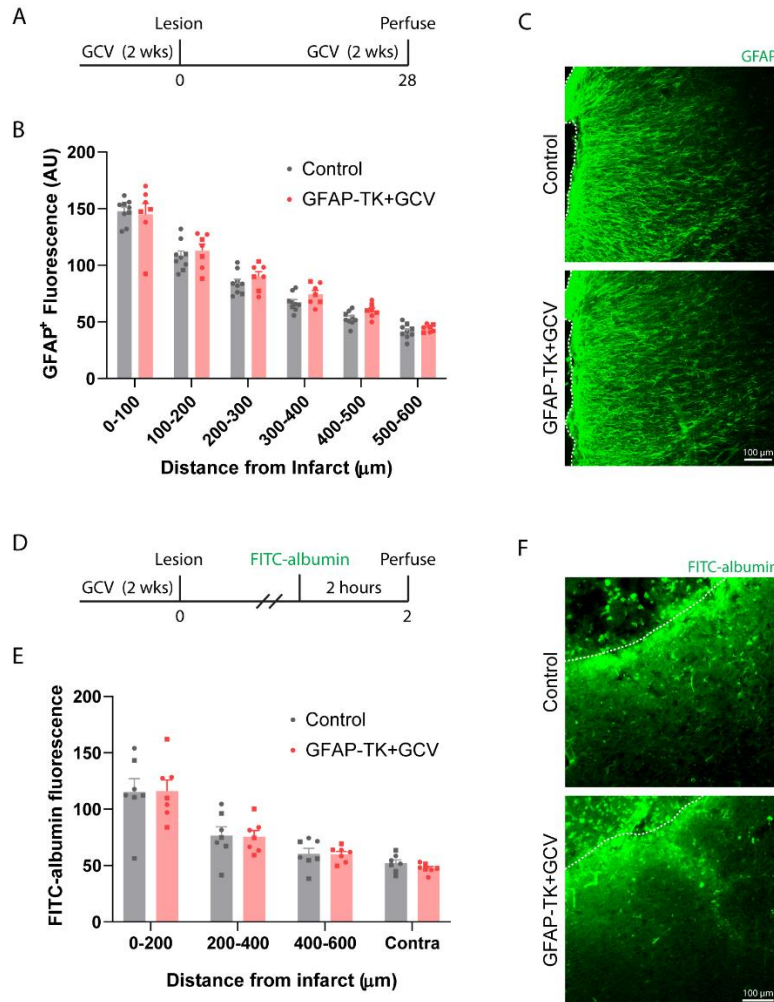
Supplemental Figure 3. Neural stem cell ablation does not alter parenchymal astrocyte reactivity or vascular permeability after stroke.

A) Experimental timeline for examining GFAP fluorescence. Tissue was obtained 28 days post-stroke (n = 9 controls (TK$^{-/-}$), n = 7 GFAP-TK$^{+/-}$). To assess parenchymal astrocyte reactivity, images were taken in superficial peri-infarct cortex where few SVZ-derived cells localize. B) GFAP$^+$ fluorescence was increased near the lesion, but declined with distance away, characteristic of astrocyte reactivity (distance effect $F(5, 84) = 172.9$, $p < 0.001$). There was no significant group effect ($F(1, 84) = 2.8$, $p = 0.100$). C) Representative images of GFAP immunostaining in peri-infarct cortex. Dashed lines indicate the lesion border. D) Experimental

947   design for examining vascular permeability. Two days post-stroke, animals were retro-orbitally

948   injected with FITC-conjugated albumin 2 hours before perfusion (n = 7 controls (TK$^{-/-}$), n = 7

949   GFAP-TK$^{+/-}$). E) FITC-albumin fluorescence was greatest near the infarct border and declined

950   with distance away, consistent with injury-induced vascular permeability (distance effect F(3,

951   48) = 36.9, p < 0.001). There was no significant effect of group (F(1, 48) = 0.07, p = 0.789). F)

952   Representative images of FITC-albumin fluorescence in peri-infarct cortex. Dashed lines

953   indicate the lesion border. Data are presented as mean ± SEM. Datapoints representing males are

954   shown as circles; datapoints representing females are shown as squares.
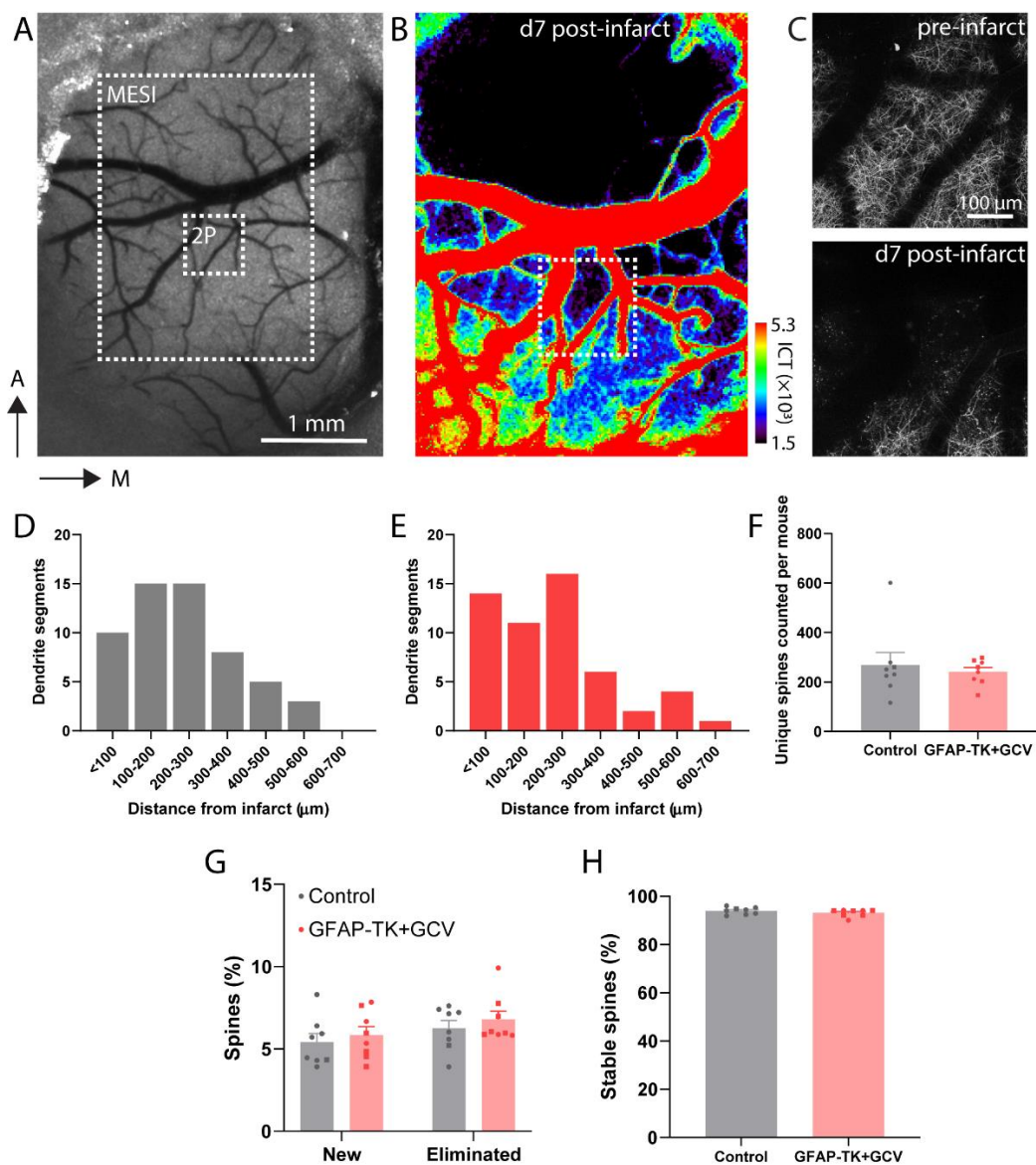
Supplemental Figure 4. Additional data 2-photon imaging data.

A) MESI accurately delineates the infarct border. Widefield laser speckle contrast image

showing the cortical surface through a cranial window. B) Multi-exposure speckle imaging

(MESI) image of blood flow corresponding to the region indicated in panel A. C) Two photon

image of GFP-labeled apical dendrites (Thy1-GFP) corresponding to the region indicated in

panels A and B. The infarct border revealed by MESI (black region in B) matches the region in

54

962   which GFP fluorescence is absent. D-E) Distribution of the locations of analyzed dendrite

963   segments relative to the infarct border for control (D) and GFAP-TK+GCV mice (E) (number of

964   segments is summed across mice). F) Numbers of unique longitudinally tracked dendritic spines

965   by group. Each point corresponds to an individual animal. Pre-stroke spine turnover (G) and

966   stability (H) were not different between groups ($t(14) \leq 1.1$, $p \geq 0.272$). Data are presented as

967   mean ± SEM. Datapoints representing males are shown as circles; datapoints representing

968   females are shown as squares.
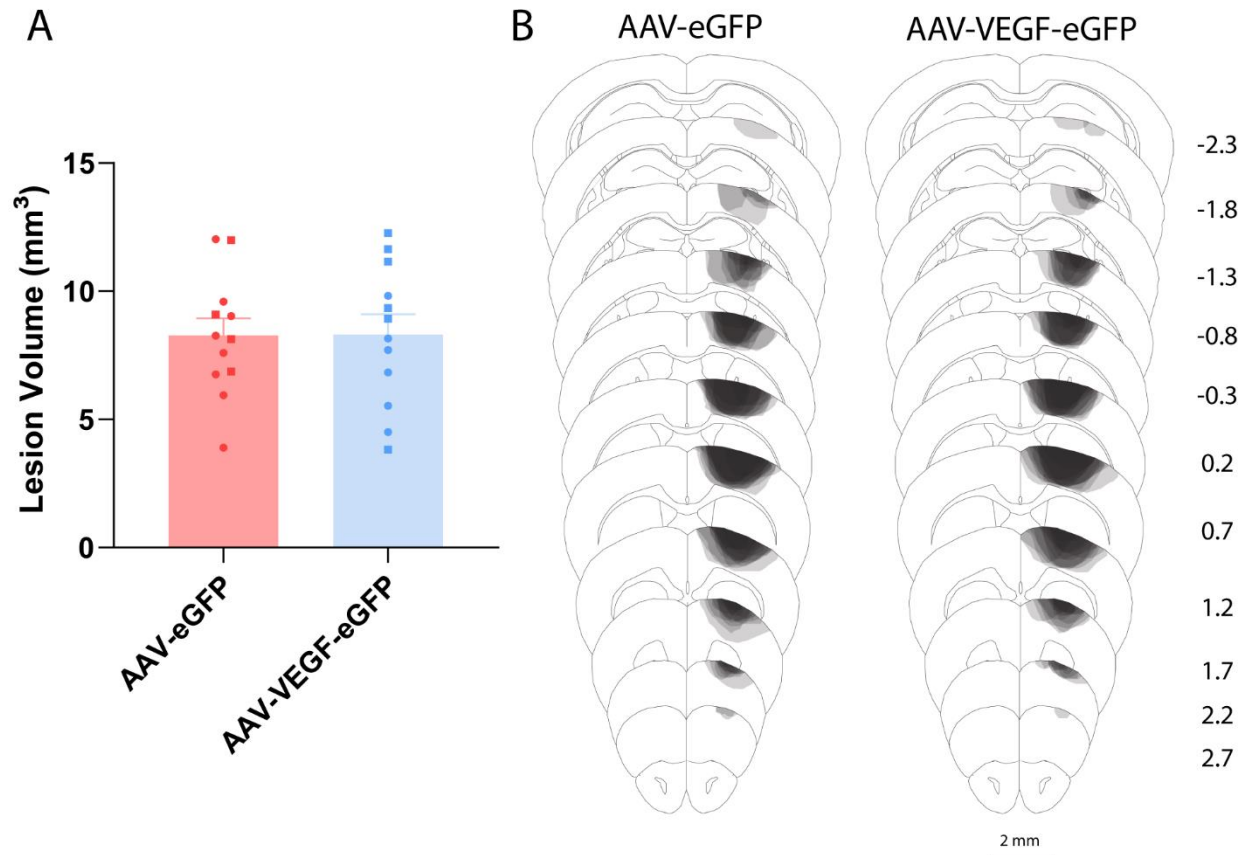
969

970
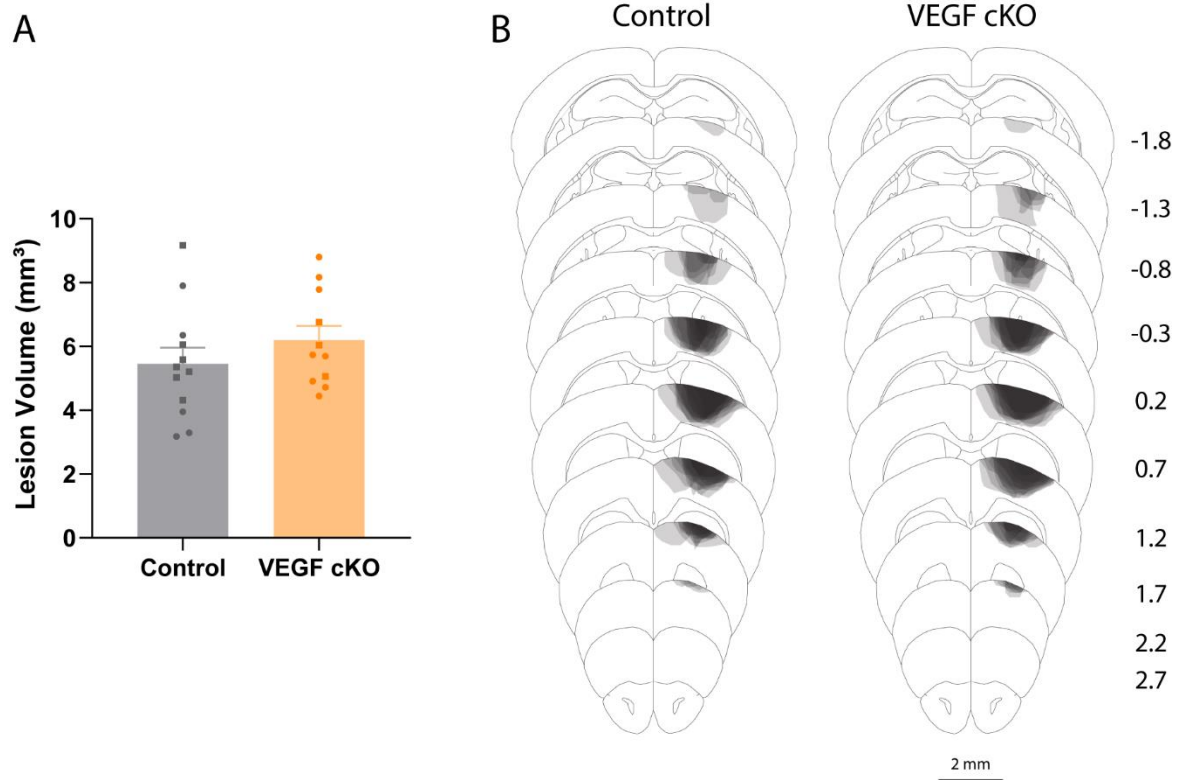
Figure S5. VEGF cKO did not affect lesion size or location.

A) Lesion size was not different between groups (t(21) = 1.08, p = 0.292). B) Lesion

reconstruction. Darker shades indicate greater overlap between animals.

974

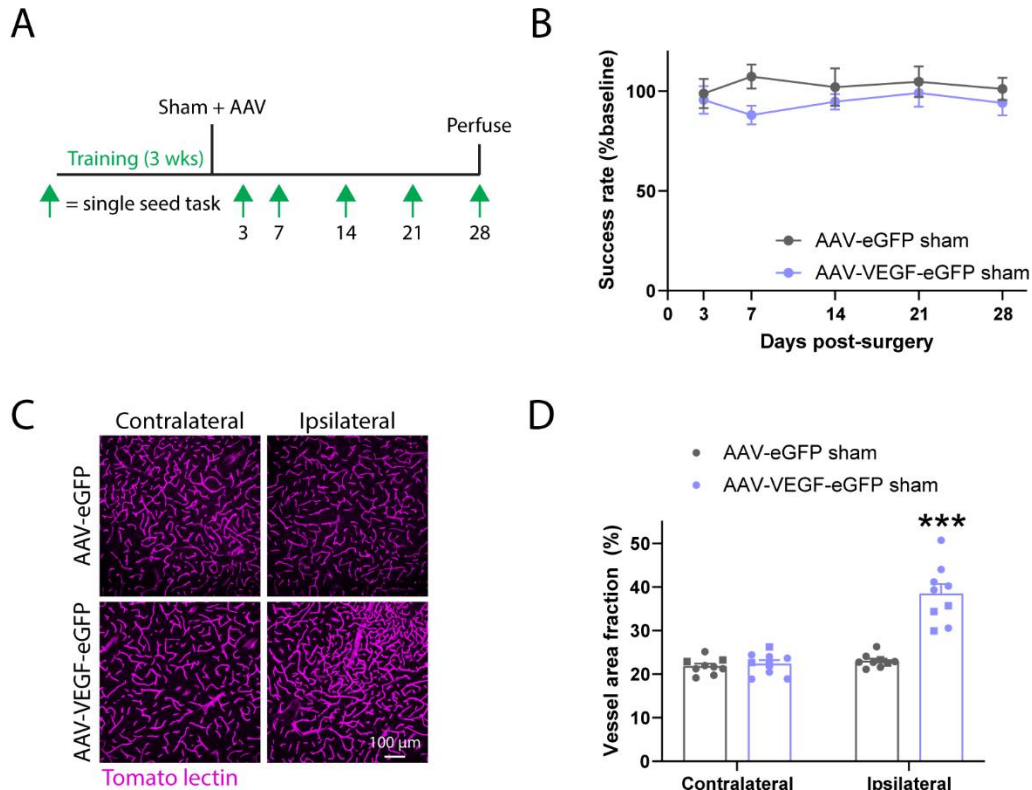**Figure S6. AAV-VEGF-eGFP did not affect lesion size or location.**

A) Lesion size was not different between groups (t(22) = 0.04, p = 0.967). B) Lesion reconstruction. Darker shades indicate greater overlap between animals.

Figure S7. AAV-VEGF-eGFP does not affect motor function in sham-operated animals.

A) Experimental timeline. Wildtype mice were trained on the single seed reaching task, subjected to a sham stroke procedure, and injected with either AAV-eGFP or AAV-VEGF-eGFP (n = 8/group). Performance on the single seed task was periodically tested up to 28 days post-surgery. B) Performance on the single seed task was not different between groups (F(1, 14) = 3.8, p = 0.071). C, D) Representative images (C) and quantification (D) of vasculature in contralateral and ipsilateral cortex (relative to AAV injection site). AAV-VEGF-eGFP increased vessel density in ipsilateral cortex (t(16) = 6.8, ***p < 0.001) (n = 9/group). Data are presented as mean ± SEM. Where individual datapoints are shown, datapoints representing males are shown as circles; datapoints representing females are shown as squares.

58

992 **Supplemental Table 1. List of reagents.**

Antibodies	Source	Identifier
Rabbit polyclonal anti-ASCL1 (1:1000)	Abcam	ab74065
Rabbit polyclonal anti-ASCL1 (1:500)	Cosmo Bio	CAC-SK-T01-003
Rabbit polyclonal anti-CD133 (1:1000)	Abcam	ab19898
Rabbit monoclonal anti-BDNF (1:1000)	Abcam	ab108319
Rabbit polyclonal anti-BrdU (1:500)	Abcam	ab152095
Rat monoclonal anti-BrdU (1:500)	Abcam	ab6326
Goat polyclonal anti-DCX (1:500)	Santa Cruz Biotech.	Sc-8066
Rabbit monoclonal anti-ERG (1:500)	Abcam	ab92513
Rabbit polyclonal anti-FGF2 (1:500)	Sigma	F-3393
Rabbit polyclonal anti-GDNF (1:100)	Abcam	ab18956
Rabbit polyclonal anti-GFAP (1:1000)	Dako	Z0334
Chicken polyclonal anti-GFP (1:5000)	GeneTex	GTX13970
Goat polyclonal anti-HSV thymidine kinase (1:1000)	Santa Cruz Biotech.	Sc-28038
Rabbit monoclonal anti-Id2 (1:1000)	CalBioreagents	M213
Rabbit polyclonal anti-Ki67 (1:500)	Abcam	ab66155
Rabbit monoclonal anti-NeuN (1:2000)	Millipore	MABN140
Rabbit polyclonal anti-Olig2 (1:1000)	Millipore	AB9610
Rabbit monoclonal anti-S100β (1:1000)	Abcam	ab52642
Rabbit polyclonal anti-Sox2 (1:1000)	Millipore	AB5603
Rabbit polyclonal anti-VEGF (1:1000)	Millipore	ABS82
Rabbit polyclonal anti-VEGF AF647 conjugate (1:1000)	Millipore	ABS82-AF647

59

Rabbit polyclonal anti-VEGF (1:250)	Sigma	07-1420
Alexa Fluor 488-conjugated donkey anti-chicken (1:500)	Jackson ImmunoResearch	703-545-155
Alexa Fluor 488-conjugated donkey anti-goat (1:500)	Jackson ImmunoResearch	705-545-147
Alexa Fluor 594-conjugated donkey anti-goat (1:500)	Jackson ImmunoResearch	705-585-147
Alexa Fluor 488-conjugated donkey anti-rabbit (1:500)	Jackson ImmunoResearch	711-545-152
Alexa Fluor 594-conjugated donkey anti-rabbit (1:500)	Jackson ImmunoResearch	711-585-152
Alexa Fluor 647-conjugated donkey anti-rabbit (1:500)	Jackson ImmunoResearch	711-605-152
Alexa Fluor 488-conjugated donkey anti-rat (1:500)	Jackson ImmunoResearch	712-545-153
Alexa Fluor 594-conjugated donkey anti-rat (1:500)	Jackson ImmunoResearch	712-585-153

Viruses	**Source**	**Identifier**
AAV5-CaMKIIa-eGFP	Addgene	50469-AAV5
AAV5-EF1α-eGFP	Addgene	105547-AAV5
AAV5-EF1α-VEGFA-P2A-eGFP	Vector Builder	N/A

Chemicals	**Source**	**Identifier**
Rose Bengal	Sigma	Cat# 330000
Bromodeoxyuridine	Sigma	Cat# B5002
FITC-conjugated albumin	Sigma	Cat# A9971
Dylight 594-conjugated tomato lectin	Vector Labs	DL-1177-1
Dylight 649-conjugated tomato lectin	Vector Labs	DL-1178-1

	Roche	N/A
Ganciclovir		
Mice	**Source**	**Identifier**
Ai14: B6.Cg-Gt(ROSA)26Sortm14(CAG-tdTomato)Hze/J	The Jackson Laboratory	JAX #007914
GFAP-TK: B6.Cg-Tg(Gfap-TK)7.1Mvs/J	The Jackson Laboratory	JAX #005698
Nestin-CreER: C57BL/6-Tg(Nes-cre/ERT2)KEisc/J	The Jackson Laboratory	JAX #016261
ASCL1-CreER: Ascl1tm1.1(Cre/ERT2)Jejo/J	The Jackson Laboratory	JAX #012882
CAG-LSL-Sun1-sfGFP: B6;129-Gt(ROSA)26Sortm5(CAG-Sun1/sfGFP)Nat/J	The Jackson Laboratory	JAX #021039
Thy1-GFP: Tg(Thy1-EGFP)MJrs/J	The Jackson Laboratory	JAX #007788
floxed Vegfa	Genentech, Gerber et al. 1999	N/A

993